Article:
Baù, D. orcid.org/0000-0002-0730-5478 (2024) Semi-analytical solutions for land subsidence due to groundwater withdrawal. Journal of Hydrology, 642. 131813. ISSN 0022-1694

https://doi.org/10.1016/j.jhydrol.2024.131813

Journal of Hydrology 642 (2024) 131813

Contents lists available at ScienceDirect

Journal of Hydrology

journal homepage: www.elsevier.com/locate/jhydrol

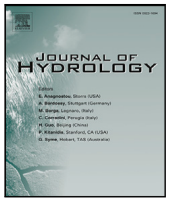

Research papers

Semi-analytical solutions for land subsidence due to groundwater withdrawal

Domenico Baù

The University of Sheffield, School of Mechanical, Aerospace and Civil Engineering, Sir Frederick Mappin Building, Mappin Street, Sheffield S1 3JD, United Kingdom

ARTICLE INFO

This manuscript was handled by Corrado Corradini, Editor-in-Chief, with the assistance of William Payton Gardner, Associate Editor.

Keywords:
Land subsidence
Nucleus of strain
Model emulators

ABSTRACT

This paper introduces novel semi-analytical models tailored for estimating land subsidence resulting from groundwater extraction in confined aquifers. These models offer high scalability, allowing them to be applied to various well configurations and pumping schedules. Their development involves the numerical integration of two key analytical solutions: the "nucleus of strain" (NoS) (Mindlin and Chen, 1950), which represents a localised zone within the aquifer where a unit change in pore pressure leads to deformation and subsequent surface displacement, and the classic Theis equation (Theis, 1935) for the pore pressure changes induced by a constant-rate well pumping from a laterally unbounded aquifer. These integrations yield surface displacement components, both horizontal and vertical, expressed as functions of two dimensionless spatial–temporal variables, which encompass aquifer depth, thickness, well placement, pumping schedules, and critical hydro-geomechanical parameters like hydraulic conductivity, porosity, vertical compressibility, and water compressibility. Proposed are two distinct modelling approaches: one employing a lookup table (LT) derived from numerical integration results, and the other providing direct closed-form surface displacement solutions by fitting LT data with "hinge models", which use piecewise-linear functions linked by sigmoidal curves for computational efficiency. In both cases, surface displacement components are estimated by plugging in the dimensionless variables. Conditions of variable pumping from multiple wells can be addressed by applying superposition of solutions. In essence, these semi-analytical models offer swift computational capabilities for understanding and forecasting land subsidence dynamics. Their scalability makes them adaptable to a wide array of well configurations and scheduling scenarios, rendering them valuable for numerous applications. They are particularly significant for providing preliminary estimates of the impacts of groundwater development, conducting "what-if" tests, and performing sensitivity analyses to identify key factors affecting land subsidence risk. This underscores the importance of these models in sustainable groundwater resource management and in mitigating land subsidence and its associated consequences.

1. Introduction

Land subsidence refers to the settling of the Earth's surface in response to various natural and human-induced factors and may occur over relatively small areas or cover large regions at various rates, from slow to rapid. One of the primary anthropogenic causes of land subsidence is the extraction of fluids from the subsurface. These activities are carried out commonly for purposes of fossil fuel and groundwater development. While groundwater resources can be found at any depth, their quality is suitable for domestic, agricultural, or industrial use normally when they are taken from shallower sedimentary formations, whose depth typically range from a few meters to a few hundred meters in depth. Excessive pumping of groundwater from aquifers is arguably the main cause of land subsidence worldwide (Gambolati et al., 1991; Holzer and Galloway, 2005; Erkens et al., 2015; Guzy and Malinowska, 2020).

Land subsidence is the effect of a consolidation process that is triggered by groundwater abstraction, which causes a reduction in fluid pressure followed by an overall aquifer compaction, under the isostatic load exerted by burying materials. Such a deformation is then gradually transferred to the surface, where settlement is observed. This effect may pose significant environmental and infrastructural risks, which highlights the need for modelling and monitoring programs that can be used to assist sustainable water management practices that mitigate the risks. These may be particularly significant in coastal regions where the ground elevation is of the order of a few tens of centimetres above the mean sea level (Abidin et al., 2015; Yan et al., 2020) as it has the

E-mail address: d.bau@sheffield.ac.uk.

https://doi.org/10.1016/j.jhydrol.2024.131813
Received 10 March 2024; Received in revised form 1 July 2024; Accepted 31 July 2024
Available online 20 August 2024

potential to significantly increase the vulnerability to sea level rise and coastal flooding (Kulp and Strauss, 2019).

Mathematical models play a crucial role in forecasting land displacement caused by groundwater withdrawal. These models can be categorised into two types: numerical and analytical. The latter relies on solving the classical equations of poro-elasticity (Biot, 1941, 1955; Verruijt, 1969) through discretisation techniques like finite elements, finite differences, finite volumes, or their combinations. These models possess considerable power and flexibility, enabling simulation of intricate hydrogeological scenarios under various conditions of heterogeneity, elasticity, elasto-plasticity, and viscosity constitutive laws. As a result, they have led to unparallelled levels of sophistication and accuracy in simulations. For in-depth examinations of numerical models, one may refer to the works of Galloway and Burbey (2011), Gambolati and Teatini (2015), and Guzy and Malinowska (2020).

Analytical models constitute the earliest group of mathematical tools for land subsidence assessment, and remain to these days an attractive solution for their ease of application, computational efficiency and low data requirement. One of the earliest and most renowned models for land subsidence was developed by Geertsma (1966, 1973) to predict surface displacement caused by a disk-shaped reservoir embedded in a homogeneous, linearly-elastic, semi-infinite domain and subjected to a constant change in pore pressure. Geerstma used the "Nucleus of Strain" (NoS) equations (Mindlin, 1936; Mindlin and Chen, 1950), integrating them over the reservoir volume. These equations quantify both horizontal and vertical displacements resulting from a unit change in pore pressure within a unit volume at a specified depth underground. Following Geertsma's work, van Opstal (1974) and, more recently, Tempone et al. (2010) proposed analytical models to estimate the surface vertical displacement assuming the reservoir is positioned above a rigid basement.

We should note that the NoS integration method can be extended to reservoirs with various shapes that experience a spatially distributed change in pore pressure, which typically requires numerical computation. However, under specific conditions, an analytical solution is feasible. For instance, Jayeoba et al. (2019) introduced an analytical solution for the surface vertical settlement above a well that pumps at a constant rate from a cylindrical reservoir. In this case, due to the radial symmetry of the pore pressure change, the integration was carried out by utilising Geertsma's vertical surface displacement at the centre of a disk-shaped reservoir.

For groundwater development applications, the studies of Bear and Corapcioglu (1981a,b) and Corapcioglu and Bear (1983) constitute the earliest examples of analytically based models for calculations of land subsidence due to pumping from shallow aquifers. Bear and Corapcioglu (1981a) derived a closed-form solution for the compaction resulting from pumping in a confined aquifer. Their derivation relied on the integration of the 3D equation of groundwater flow across the aquifer's thickness and the introduction, through Terzaghi's effective stress principle (Terzaghi, 1923; Terzaghi and Peck, 1967), of a linear-elastic constitutive model between the vertical aquifer compaction and the average piezometric head, assuming horizontal flow and no horizontal displacements.

Bear and Corapcioglu (1981b) integrated the 3D classical equations of poro-elasticity (Biot, 1941) within the aquifer thickness, considering shear-free boundaries and conditions of plane stress, still under the assumption of horizontal flow and linear-elastic stress–strain relations. They thus derived closed-form equations for both vertical and horizontal displacements associated with flow to pumping wells in confined and partially confined aquifers. Corapcioglu and Bear (1983) extended the approach of Bear and Corapcioglu (1981b) to the case of unconfined aquifers. In this scenario, applying Terzaghi's principle requires considering the variation in total stress to link changes in water level to effective stress variations.

It is worth highlighting that the solutions presented by Bear and Corapcioglu primarily focus on estimating the aquifer deformation (consolidation settlement) rather than directly calculating surface displacements. Indeed, the solutions are integrated over the saturated aquifer thickness, assuming a rigid basement beneath the aquifer. As a result, strains in the aquifer underburden and overburden are not taken into account, and the formation depth results to have no impact on the surface displacement.

In the work of Xie et al. (2014), Biot's equations of poro-elasticity were solved analytically to determine radial symmetric analytical solutions for the land surface displacement induced by the deformation of an overburden layer sitting above a confined aquifer. Such a solution, however, did not account for the compaction of the aquifer, which was assumed merely as a rigid boundary where a time-dependent change in fluid pressure is imposed. Such a "drawdown" was given by the Theis solution (1935) for a single well pumping continuously in a laterally-infinite, horizontal and constant-thickness confined aquifer.

Loáiciga (2013) provided closed-form analytical solutions for the vertical consolidation settlement occurring within both confined and unconfined aquifers due to groundwater pumping, considering conditions of both steady-state and transient flow. These solutions were derived by integrating traditional aquifer drawdown solutions, such as in Thiem (1906) and Theis (1935), across the aquifer thickness. Loáiciga's approach enabled the estimation of effective stress variations that result in aquifer compaction, applicable to both normally consolidated and under-consolidated basins, and made use of linear superposition of solutions to simulate the effect of multiple wells.

Of related interest is the work of Pujades et al. (2017), who used a numerical approach to analyse the strain caused by groundwater pumping in overconsolidated, perfectly confined and partially confined aquifers. Their investigation employed a radial-symmetric conceptual model similar to the one used by Bear and Corapcioglu (1981b) and addressed various aspects, including the influence of boundary conditions on displacements at the aquifer's bottom and lateral boundaries. They also developed a closed-form solution for aquifer compaction in the case of confined flow, which significantly expanded upon the one proposed by Bear and Corapcioglu (1981b) for three-dimensional consolidation.

Zhang and Mehrabian (2020) presented an analytical solution to the problem of underground fluid injection in a disk-shaped reservoir while accounting for strain-induced changes in permeability. While the focus of such a study was on aquifer injectivity rather than surface displacement, the rock stress was assumed to be a function of the pore fluid pressure change within the reservoir and was derived by integration of the NoS solution in an elastic half space. Wang et al. (2022) presented a semi-analytical solution for the land subsidence due to pressure changes in a poro-elastic reservoir. Their method was based on the integration of a Green function derived as the solution of the coupled hydro-geomechanical system equation, multiplied to the reservoir pressure variation obtained from a flow simulator, either numerical or analytical.

Aligned with the works reviewed above, this paper presents computationally fast semi-analytical models that can be used to assess land surface displacement due to aquifer pumping. These models effectively merge the NoS solution with the classic Theis solution for flow to wells in confined aquifers, following an approach that, to the best of the Author's knowledge, is fully original. Despite both solutions being analytically based, their coupling results in integrals that can only be calculated numerically, which is computationally expensive.

To overcome these limitations, two distinct models are proposed here, one employing lookup tables (LTs) and another relying on direct closed-form solutions, which furnish precise outputs for the horizontal and vertical components of the surface displacement. The closed-form solution relies on the fitting of the LT data with "hinge" models, that is, a particular type of piecewise-linear functions connected by smoothing curves around the intersection points. Both models share the same fundamental inputs, which are reduced to two dimensionless

parameters, encompassing aquifer depth and thickness, surface location, well locations, time since pumping initiation, and critical hydro-geomechanical properties, including hydraulic conductivity, porosity, vertical compressibility and water compressibility.

By adopting the NoS approach, these models enable a comprehensive analysis of 3D deformation effects across the aquifer, and the underburden and overburden formations. These models prioritise efficiency and scalability. By applying the principle of superposition, they enable the user to simulate land subsidence induced by multiple well pumping scenarios and varying pumping rates. These developments represent a notable step forward in the realm of land subsidence prediction, offering versatility and computational efficiency.

This paper is organised as follows: Section 2 describes the fundamentals of the land subsidence model and the NoS solution; Section 3 presents the derivation of the semi-analytical land subsidence simulators, which rely on the integration of the NoS solution with the Theis equation over the aquifer volume, and the parameterisation of these integrals with respect to two dimensionless variables; Section 4 present the results of a number of numerical tests conducted for model testing purposes; in Section 5, a discussion is provided concerning the model's capabilities, along with a concise overview of its fundamental assumptions and an examination of the constraints imposed on the model's accuracy and relevance; Section 6 includes concluding remarks on the models developed.

2. Land Subsidence Model

Considered here is the case of a geomechanically homogeneous, linearly-elastic, semi-infinite system delimited by a traction-free horizontal surface, and subject to a spatially distributed pore pressure change Δp within a volume Ω embedded in it. Based on the superposition principle, the components u_x, u_y, and u_z of the surface displacement along the coordinate directions x, y and z, and at a generic time t, are given by the following volume integrals:

$$\begin{aligned} u_x(x,y,t) &= \int_\Omega u_h^*(r,c)\cdot\eta_x\cdot\Delta p\cdot d\Omega \\ u_y(x,y,t) &= \int_\Omega u_h^*(r,c)\cdot\eta_y\cdot\Delta p\cdot d\Omega \\ u_z(x,y,t) &= \int_\Omega u_v^*(r,c)\cdot\Delta p\cdot d\Omega \end{aligned} \tag{1}$$

where: $\Delta p=\Delta p\left(x',y',c,t\right)\left[\mathrm{MT^{-2}L^{-1}}\right]$ with $\left(x',y',c\right)\in\Omega$ and $d\Omega=dx'\cdot dy'\cdot dc$; r and (η_x,η_y) are the length and the cosine directors of the 2D vector $\left(x-x',y-y'\right)$, respectively; and u_h^* and u_v^* are "Green" functions that represent the horizontal and vertical displacements, respectively, associated with a "Nucleus of Strain" (NoS), that is, a unit volume located at depth c, in which a unit change in pore pressure takes place (Fig. 1a).

Eqs. (1) represent the solution to the classic equations of poro-elasticity (Biot, 1941) under the assumption that the flow field is "one-way" coupled to the deformation of the porous medium (Verruijt, 1969). In the case of a homogeneous porous medium, closed-form analytical expressions of the Green functions (u_h^*,u_v^*) have been derived by Mindlin and Chen (1950) and Geertsma (1973):

$$\begin{aligned} &\text{(a):}\quad u_h^*(r,c)=\frac{c_M\cdot(1-\nu)}{\pi}\cdot\frac{r}{\left(c^2+r^2\right)^{1.5}} \\ &\text{(b):}\quad u_v^*(r,c)=\frac{c_M\cdot(1-\nu)}{\pi}\cdot\frac{c}{\left(c^2+r^2\right)^{1.5}} \end{aligned} \tag{2}$$

where c_M and ν are the vertical compressibility $\left[\mathrm{M^{-1}T^2L}\right]$ and the Poisson ratio $[/]$ of the porous medium, respectively, and r is the radial coordinate with respect to a vertical axis crossing the NoS location (Fig. 1a). Note that since $u_h/u_v=r/c$, u_h and u_v are equal for $r=c$.

Eqs. (2) can be made dimensionless by normalising them with respect to the displacement $u_v^*(0,c)=\frac{c_M\cdot(1-\nu)}{\pi\cdot c^2}\left[\mathrm{M^{-1}T^2L^{-1}}\right]$, and introducing the scaled radial coordinate $R=r/c$, which leads to the following expressions:

$$\begin{aligned} &\text{(a):}\quad \overline{u_h}^*(R)=\frac{u_h^*(r,c)}{u_v^*(0,c)}=R\cdot\left(1+R^2\right)^{-1.5} \\ &\text{(b):}\quad \overline{u_v}^*(R)=\frac{u_v^*(r,c)}{u_v^*(0,c)}=\left(1+R^2\right)^{-1.5} \end{aligned} \tag{3}$$

Eqs. (3) show that the normalised displacement depends solely on the scaled radial coordinate R, and is thus invariant with respect to the NoS depth c. The normalised displacement components $(\overline{u_h}^*,\overline{u_v}^*)$ are graphed in Fig. 1b.

3. Surface Displacements due to Groundwater Pumping

Eqs. (1) can be used to estimate the surface displacement components if the pore pressure change field $\Delta p\left(x',y',z',t\right)$ is known. This field may be obtained using a groundwater flow model, and the integrals (1) are then calculated numerically by discretising the domain Ω into a finite-element (FE) or finite-difference (FD) grid of N_e elements or cells, which allows for splitting them into the sum of as many terms. By referring the surface displacements to the N_n nodes of a surface grid, Eqs. (1) may be expressed as a matrix–vector product (Verrujit, 2015):

$$\begin{bmatrix}\mathbf{U}_x\\ \mathbf{U}_y\\ \mathbf{U}_z\end{bmatrix}=\begin{bmatrix}\mathbf{M}_x\\ \mathbf{M}_y\\ \mathbf{M}_z\end{bmatrix}\cdot\mathbf{F} \tag{4}$$

where: $\mathbf{U}_x$, $\mathbf{U}_y$ and $\mathbf{U}_y$ are $N_n\times 1$ vectors including the displacement components at the surface points; $\mathbf{F}$ is a $N_e\times 1$ vector, whose generic jth component equals the product $V_j\cdot\Delta p_j$, where V_j is the volume of element j ($j=1,..,N_e$), and Δp_j is average pore pressure change in it; $\mathbf{M}_x$, $\mathbf{M}_y$, and $\mathbf{M}_z$ are $N_n\times N_e$ matrices, whose generic $m_{i,j}$ coefficient depends on the NoS surface displacements (Eqs. (2)) for the radial distance $r_{i,j}$ between the grid node i ($i=1,..,N_n$) and element j's centroid, and element j's depth c_j.

An alternative "hybrid" semi-analytical approach, is here devised in the case of the pore pressure change Δp produced by a single well, operating at a constant rate Q within a confined, laterally-infinite, homogeneous, isotropic and horizontal aquifer. The well is positioned at the origin of the coordinate system ($x=0, y=0$) (Fig. 2) and is fully-screened through the aquifer, which is located at average depth c and has a thickness b. Under these conditions, the change in pore pressure in the aquifer can be calculated as Theis (1935):

$$\Delta p\left(x',y',z',t\right)=\rho_w\cdot g\cdot\frac{Q}{4\cdot\pi\cdot b\cdot K}\cdot W\left(\frac{S_s}{4\cdot K}\cdot\frac{r'^2}{t}\right) \tag{5}$$

where ρ_w is the water density $\left[\mathrm{ML^{-3}}\right]$, g is the standard gravity $\left[\mathrm{LT^{-2}}\right]$, Q is the well flow rate (negative for extraction) $\left[\mathrm{L^3T^{-1}}\right]$, K is the aquifer hydraulic conductivity $\left[\mathrm{LT^{-1}}\right]$, S_s is the specific elastic storage $\left[\mathrm{L^{-1}}\right]$, and r' is the radial distance from the well [L], which is equal to $\sqrt{x'^2+y'^2}$ (Fig. 2). The coefficient S_s is linked to the compressibility by the classic relationship (De Wiest, 1966):

$$S_s=\rho_w\cdot g\cdot\left(c_M+\phi\cdot c_w\right) \tag{6}$$

where ϕ is the aquifer porosity $[/]$, and c_w is the water compressibility $\left[\mathrm{M^{-1}T^2L}\right]$. In Eq. (5), $W(\cdot)$ is a "well function" $[/]$, given by:

$$W(u)=\int_u^{+\infty}\frac{e^{-u'}}{u'}\cdot du' \tag{7}$$

where $u=\frac{S_s}{4K}\cdot\frac{r'^2}{t}$ $[/]$. The "exponential" integral in Eq. (7) is typically calculated numerically using a truncated form of the series $-0.57721566-ln(u)-\sum_{i=1}^{+\infty}\frac{(-1)^i u^i}{i\ i!}$. Note that Eq. (5) is valid for $c-b/2\le z'\le c+b/2$, otherwise $\Delta p=0$.

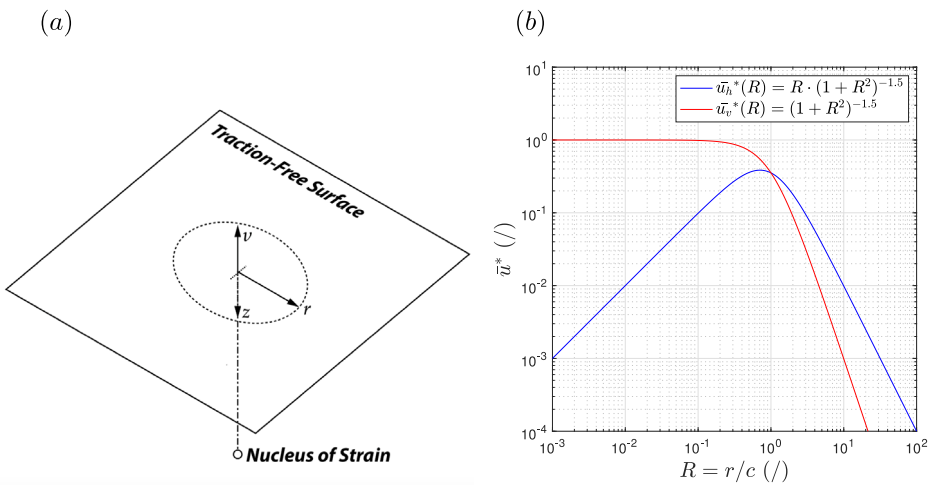

Fig. 1. (a) 3D semi-infinite space including the NoS; (b) Horizontal and vertical components of the normalised surface displacement vs. the radial distance r scaled with respect to the depth c for a NoS within a semi-infinite homogeneous porous medium.

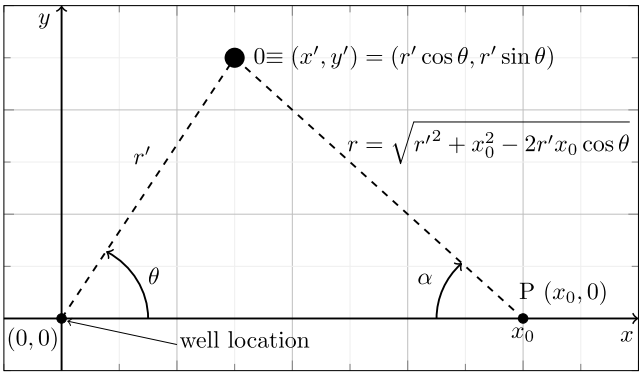

Fig. 2. Reference system adopted for the derivation of the surface displacements associated with the Theis (1935) analytical solution. The pumping well is situated at the origin, the generic observation point P is on the x-axis, whereas the integration moving point O is located at the generic polar coordinates (r', θ).

Since the well is located at the origin of the cartesian system (Fig. 2), the displacement is radial-symmetric with respect to the (vertical) z axis, and thus the calculation is limited to the displacement components u_x and u_z at any point P on the x axis, having the generic radial coordinate x_0 (Fig. 2). Substituting Eqs. (2) and (5) in Eq. (1), and adopting the polar coordinate system (r', θ) shown in Fig. 2, leads to the following expressions for the radial and vertical displacement components:

$$
\begin{aligned}
u_h(x_0,t) &= u_v^* \cdot \int_0^{+\infty} W(\alpha \cdot r'^2) \\
&\quad \left[\int_0^{2\pi} \frac{x_0 - r' \cdot \cos\theta}{\left(c^2 + r'^2 + x_0^2 - 2 \cdot r' \cdot \cos\theta\right)^{1.5}} \cdot d\theta \right] \cdot r' \cdot dr' \\
u_v(x_0,t) &= u_v^* \cdot \int_0^{+\infty} W(\alpha \cdot r'^2) \\
&\quad \left[\int_0^{2\pi} \frac{c}{\left(c^2 + r'^2 + x_0^2 - 2 \cdot r' \cdot \cos\theta\right)^{1.5}} \cdot d\theta \right] \cdot r' \cdot dr'
\end{aligned}
\tag{8}
$$

where $u_v^* = \frac{c_M \cdot (1-\nu) \cdot \rho_w \cdot g \cdot Q}{4 \cdot \pi^2 \cdot K}$ [L], and $\alpha = \frac{S_s}{4 \cdot K \cdot t}$ $\left[\mathrm{L}^{-2}\right]$ (*i.e.* $\alpha \cdot r'^2 = u$). Eqs. (8) can be further modified by scaling the radial coordinate r' to the depth c, and dividing them by u_v^*, which yields:

$$
\begin{aligned}
\overline{u_h}(X_0, \beta) &= \frac{u_h(x_0,t)}{u_v^*} = \int_0^{+\infty} W(\beta \cdot R'^2) \cdot h(X_0, R') \cdot R' \cdot dR' \\
\overline{u_v}(X_0, \beta) &= \frac{u_v(x_0,t)}{u_v^*} = \int_0^{+\infty} W(\beta \cdot R'^2) \cdot v(X_0, R') \cdot R' \cdot dR'
\end{aligned}
\tag{9}
$$

with $\beta = \frac{S_s}{4K} \cdot \frac{c^2}{t}$ $[/]$ (*i.e.* $\beta \cdot R'^2 = u$) and $X_0 = x_0/c$. The two functions $h(\cdot)$ and $v(\cdot)$ are given by:

$$
\begin{aligned}
h(X_0, R') &= \int_0^{2\pi} \frac{X_0 - R' \cdot \cos\theta}{(1 + R'^2 + X_0^2 - 2 \cdot R' \cdot \cos\theta)^{1.5}} \cdot d\theta \\
v(X_0, R') &= \int_0^{2\pi} \frac{1}{(1 + R'^2 + X_0^2 - 2 \cdot R' \cdot \cos\theta)^{1.5}} \cdot d\theta
\end{aligned}
\tag{10}
$$

Eqs. (9) are useful to investigate the dependency of the scaled surface displacement $(\overline{u_h}, \overline{u_h})$ on the system parameters K, c_M, ν, and c and the independent variables x_0 and t. Note that the spatial and the temporal variables are accounted for in X_0 and β, respectively.

Since the double integrals (9)–(10) cannot be solved analytically, they are calculated numerically using the iterative quadrature method developed by Shampine (2008a,b). The results of these integrations are given in Fig. 3, which shows a series of profiles of the scaled displacement components $(\overline{u_h}, \overline{u_v})$ as functions of the spatial variable X_0, for a discrete set of values of the temporal variable β. A sensitivity analysis (not presented here) conducted on $\beta = \frac{S_s}{4K} \cdot \frac{c^2}{t}$ indicates that such a variable typically takes values between 10^{-8} and 10, which is the range considered in Fig. 3.

In Fig. 3, the scaled displacement components $(\overline{u_h}, \overline{u_v})$ are seen to generally increase as β decreases, that is, they become expectedly more pronounced at larger times, and for shallower aquifers, having lower c. In addition, the displacements result larger for systems with lower values of the ratio S_s/K, that is, with low-compressibility c_M (see Eq. (6)) and high-permeability K. This may seem counterintuitive at a first glance, but one must bear in mind that $\overline{u_h}$ and $\overline{u_v}$ are scaled with respect to the coefficient u_v^* which is linearly proportional to c_M/K, thus what is true for the scaled displacement (Eqs. (9)) is not necessarily true for the absolute displacement (Eqs. (8)).

3.1. Lookup Table Numerical Model

The substitution of Eqs. (9)–(10) in Eqs. (8) provides the mathematical model:

$$
\begin{aligned}
u_h(x_0,t) &= \frac{c_M \cdot (1-\nu) \cdot \rho_w \cdot g \cdot Q}{4 \cdot \pi^2 \cdot K} \cdot \overline{u_h}(X_0, \beta) \\
u_v(x_0,t) &= \frac{c_M \cdot (1-\nu) \cdot \rho_w \cdot g \cdot Q}{4 \cdot \pi^2 \cdot K} \cdot \overline{u_v}(X_0, \beta)
\end{aligned}
\tag{11}
$$

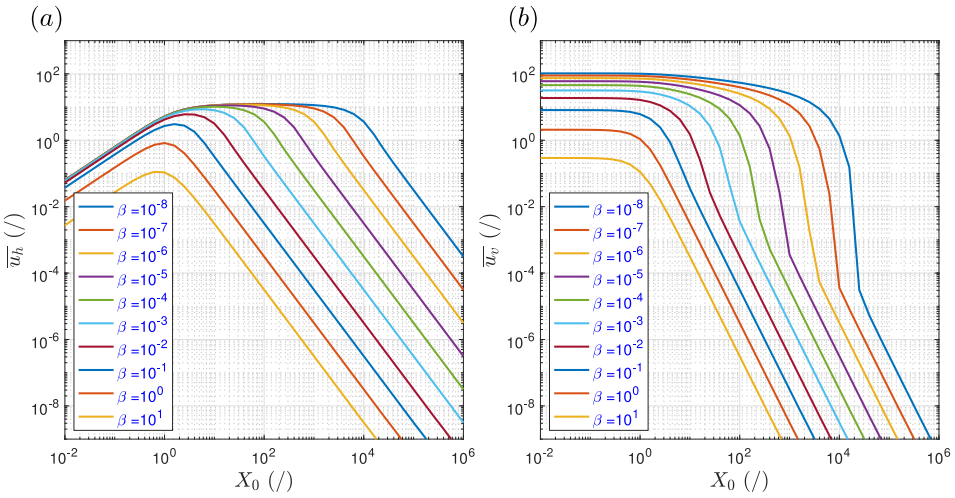

Fig. 3. Profiles of the scaled displacement components $\overline{u_h}$ (subpanel (a)) and $\overline{u_v}$ (subpanel (b)) (see Eqs. Eq. (9)) vs. the scaled radial coordinate X_0, for a discrete set of the temporal variable β, ranging between 10^{-8} and 10 with log-intervals of 1.

which simulates the surface displacement at the radial coordinate x_0 and at the time t induced by a well pumping at the constant rate Q from an aquifer of depth c, thickness b, hydraulic conductivity K and compressibility c_M. Since, as previously mentioned, the integrals (9)–(10) can only be calculated numerically, which turns out to be computationally quite expensive, it is necessary to devise approaches to overcome this limitation.

A first method presented here relies on the use of "lookup" tables (LT's), compiled by numerical calculation of the functions $\overline{u_h}(X_0,\beta)$ and $\overline{u_v}(X_0,\beta)$ (Eqs. (9)–(10)) over the points of a regular grid in the (X_0,β) space. LT's are reported in Tables A.1 and A.2 of Appendix A, which contain the datasets employed to plot Fig. 3. X_0's and β's are tabulated in the first column and in the first row, respectively, and the function values are in the table cells. Since X_0, β, $\overline{u_h}$ and $\overline{u_v}$ values may differ by several orders of magnitude, a logarithmic transformation is applied to all entries, which makes the data easier to interpret.

Based on LT data, for any generic "input" point $[\log(X_0),\log(\beta)]$, it is then possible to calculate approximate displacement components $\left[\log\left(\hat{\overline{u_h}}\right),\log\left(\hat{\overline{u_h}}\right)\right]$ by 2D interpolation. In this case, either cubic spline (de Boor, 1978) or cubic Hermite (Akima, 1974) algorithms can be adopted, both of which conserve continuity in the partial derivatives and closely adhere to the values of the original data points. Numerical tests, not presented here, indicate that a more simple bilinear interpolation method (Abramowitz and Stegun, 1964) is also viable but leads to results of comparable accuracy only if the grid resolution adopted in Tables A.1 and A.2 is at least doubled for the $\log(\beta)$ "coordinate" (*e.g.* $-8,-7.5,-7,\ldots,0.1,0.5,1,5,10$).

3.2. Closed-Form Hinge Model

An alternative to the LT model is to develop closed-form emulators $\hat{\overline{u_h}}(X_0,\beta)$ and $\hat{\overline{u_v}}(X_0,\beta)$ of $\overline{u_h}$ and $\overline{u_v}$ by regression of the LT "data". Since all profiles in Fig. 3, which are based on the data in Tables A.1 and A.2, may be interpreted as contour lines of β in the spaces of $(X_0,\overline{u_h})$ (Fig. 3a) and $(X_0,\overline{u_v})$ (Fig. 3b) and these exhibit a locally linear behaviour, it appears possible to construct semi-analytical models by fitting each profile to a "continuous hinge function".

A hinge function $h(x')$ (x' is a generic independent variable) is a type of 1D piecewise-linear function formed by merging together a generic number N of straight lines using "sigmoids" to smooth out the discontinuity in the derivative at the intersection points (Sanchez-Ubeda and Wehenkel, 1998). Indicating with $s_i(x')=q_i+m_ix'$ $(i=1,\ldots,N)$ the equation of the generic straight line, $h(x')$ may be expressed as:

$$h(x')=q_1+m_1\cdot x'+\sum_{i=2}^{N}\Delta m_{i-1,i}\cdot\Delta_{i-1,i}\cdot\log\left(1+10^{\frac{x'-x'_{i-1,i}}{\Delta_{i-1,i}}}\right) \tag{12}$$

where $\Delta m_{i-1,i}=m_i-m_{i-1}$ is the slope variation between two consecutive segments "$i-1$" and "i", $x'_{i-1,i}$ is the abscissa of their intersection point ($x'_{i-1,i}=-\frac{q_i-q_{i-1}}{m_i-m_{i-1}}$), and $\Delta_{i-1,i}$ is a smoothness coefficient. A detailed derivation of Eq. (12) is given in Appendix B.

The "goodness of fit" that can be achieved with the hinge model (12) strongly depends on the selected number of segments N. Based on the profiles in Fig. 3, it appears reasonable, for any given β value, to choose $N=3$ for $\overline{u_h}$ and $N=4$ for $\overline{u_v}$. Fig. 4 shows hinge examples that mimic the profile shapes in Fig. 3. Since Fig. 3 use a logarithmic scale on both axes, the variables in the hinge model (12) need to be log-transformed ($x'=\log X_0$, $h=\log\overline{u}$) prior to the fitting analysis. In the case of $\overline{u_h}$, the adopted hinge model results (Eq. ((B.6) in Appendix B):

$$\hat{\overline{u_h}}(X_0,\beta)=\frac{10^{q_1^{(h)}}\cdot X_0}{\left[1+\left(\frac{X_0}{X_{0_{1,2}}^{(h)}}\right)^{\frac{1}{\Delta_{1,2}^{(h)}}}\right]^{\Delta_{1,2}^{(h)}}\cdot\left[1+\left(\frac{X_0}{X_{0_{2,3}}^{(h)}}\right)^{\frac{1}{\Delta_{2,3}^{(h)}}}\right]^{2\cdot\Delta_{2,3}^{(h)}}} \tag{13}$$

whereas, in the case of $\overline{u_v}$, the hinge model is (Eq. ((B.7) in Appendix B):

$$\hat{\overline{u_v}}(X_0,\beta)=10^{q_1^{(v)}}\cdot\prod_{i=2}^{4}\left[1+\left(\frac{X_0}{X_{0_{i-1,i}}^{(v)}}\right)^{\frac{1}{\Delta_{i-1,i}^{(v)}}}\right]^{\Delta m_{i-1,i}^{(v)}\cdot\Delta_{i-1,i}^{(v)}} \tag{14}$$

Details of the derivation of Eqs. (13)–(14) are included in Appendix B.

3.2.1. Parameter Fitting

The hinge functions (13) and (14) depend on the parameter sets $\boldsymbol{\theta}_h\equiv\left[q_1^{(h)},X_{0_{1,2}}^{(h)},X_{0_{2,3}}^{(h)},\Delta_{1,2}^{(h)},\Delta_{2,3}^{(h)}\right]$ and $\boldsymbol{\theta}_v\equiv\left[q_1^{(v)},\left(X_{0_{i,i+1}}^{(v)},\Delta m_{i,i+1}^{(v)},\Delta_{i,i+1}^{(v)}\right)_{i=1,2,3}\right]$, respectively, which, based on Fig. 3, are to be considered non-linear functions of β. Here, these functions are "emulated" by fitting the models (13)–(14) to each of the profiles in Fig. 3a and b. This is carried out by implementing a two-stage regression procedure.

The first stage consists of the calculation of parameter sets that provide a best fit of the hinge models (13) and (14) for each of the 10 β values selected in Fig. 3. In practice, this requires minimising the square residuals between the hinge models (13) and (14) and the scaled surface displacement calculated over N_s points spanning the practical range of variability of X_0 (Fig. 3). These non-linear regressions are performed by using a "trust-region-reflective" algorithm (Coleman and Li, 1996) and produce 10 "training" data for each fitting parameter in $\boldsymbol{\theta}_h$ and in $\boldsymbol{\theta}_v$.

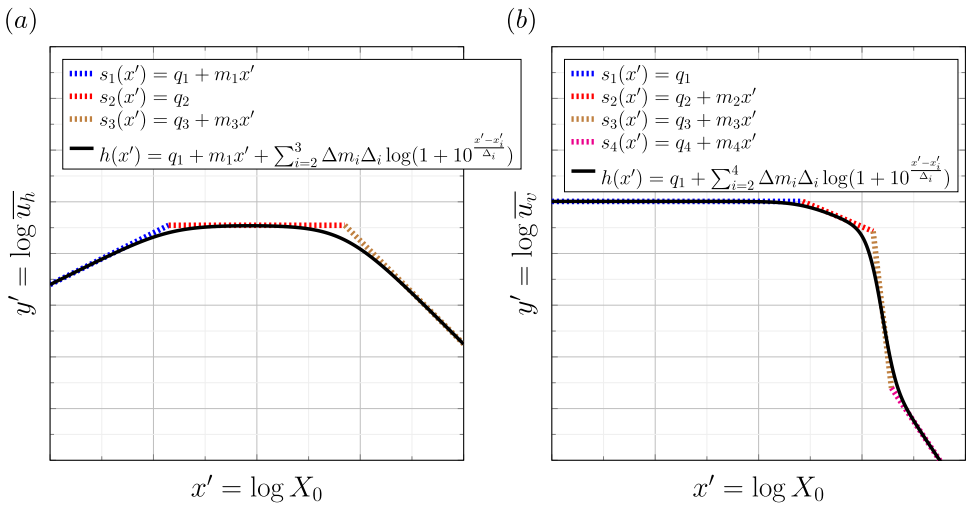

Fig. 4. Graph of the hinge functions adopted to mimic the profiles of the displacement components $\overline{u_h}$ (subpanel (a)) and $\overline{u_v}$ (subpanel (b)) vs. the scaled radial coordinate X_0 as indicated in Fig. 3. For the horizontal and the vertical components, hinge models based on $N = 3$ and $N = 4$ straight lines are selected, respectively, in the double-log space.

Table 1
Coefficients for the logarithmic hinge functions, either $g_1(\beta)$ or $g_2(\beta)$ (Eqs. (15)), defining the dependence on β of each of the parameters in $\left[q_1^{(h)}, X_{0_{1,2}}^{(h)}, X_{0_{2,3}}^{(h)}, \Delta_{1,2}^{(h)}, \Delta_{2,3}^{(h)}\right]$. These functions are used in Eq. (13) to construct the hinge model $\hat{\overline{u_h}}(X_0, \beta)$.

Fitting parameter →	$q_1^{(h)}(\beta)$	$X_{0_{1,2}}^{(h)}(\beta)$	$X_{0_{2,3}}^{(h)}(\beta)$	$\Delta_{1,2}^{(h)}(\beta)$	$\Delta_{2,3}^{(h)}(\beta)$
Hinge model →	g_1	g_2	g_2	g_1	g_1
N	2	3	2	3	4
ξ_1	0.7979	0.2992	−0.2221	0.7009	0.3452.
η_1	0.0000	0.0000	−0.4896	0.0000	0.0000.
$\Delta\eta_{1,2}$	−1.2700	−0.6250	0.4896	−0.4072	−0.0482
$\Delta\eta_{2,3}$	–	0.6250	–	0.4072.	0.4954
$\Delta\eta_{3,4}$	–	–	–	–	−0.4472
$\delta_{1,2}$	1.9270	3.7870	1.9830	4.4340	2.6280
$\delta_{2,3}$	–	1.4960	–	2.7870	1.1470
$\delta_{3,4}$	–	–	–	–	1.0110
$\beta_{1,2}$	1.5926	1.5428	0.1610	0.0547	3.97×10^{-6}
$\beta_{2,3}$	–	7.7983	–	0.4944	0.3346
$\beta_{3,4}$	–	–	–	–	1.1992

In the second stage, these training data are used to capture the relationships between the fitting parameters and the variable β. The fitting model adopted in this stage relies either on logarithmic or double-logarithmic hinge functions (Eqs. (B.4)–(B.5) in Appendix B), given as:

$$g_1(\beta) = \xi_1 + \eta_1 \cdot \log\beta + \sum_{i=2}^{N} \Delta\eta_{i-1,i} \cdot \delta_{i-1,i} \cdot \log\left[1 + \left(\frac{\beta}{\beta_{i-1,i}}\right)^{\frac{1}{\delta_{i-1,i}}}\right]$$
$$g_2(\beta) = 10^{\xi_1} \cdot \beta^{\eta_1} \cdot \prod_{i=2}^{N}\left[1 + \left(\frac{\beta}{\beta_{i-1,i}}\right)^{\frac{1}{\delta_{i-1,i}}}\right]^{\Delta\eta_{i-1,i}\cdot\delta_{i-1,i}} \quad (15)$$

The regression coefficients (ξ_1, η_1), $(\Delta\eta_{1,2}, \ldots, \Delta\eta_{N-1,N})$, $(\delta_{1,2}, \ldots, \delta_{N-1,N})$, and $(\beta_{1,2}, \ldots, \beta_{N-1,N})$ in Eqs. (15) are determined by applying a non-linear least-square regression method based on the Levenberg–Marquardt algorithm (Levenberg, 1944; Marquardt, 1963). Results of the two-stage process are presented in Tables 1 and 2 for the coefficients in θ_h and θ_v, respectively. Further details on the procedure may be found in Appendix B.

In summary, the integrals providing the scaled displacement components $\overline{u_h}$ and $\overline{u_v}$ (Eqs. (9)–(10)) are approximated by the closed-form hinge models $\hat{\overline{u_v}}(X_0, \beta)$ (Eqs. (13)) and $\hat{\overline{u_v}}(X_0, \beta)$ (Eqs. (14)) with the parameters $\left[q_1^{(h)}, X_{0_{1,2}}^{(h)}, X_{0_{2,3}}^{(h)}, \Delta_{1,2}^{(h)}, \Delta_{2,3}^{(h)}\right]$ and $\left[q_1^{(v)}, \left(X_{0_{i,i+1}}^{(v)}, \Delta m_{i,i+1}^{(v)}, \Delta_{i,i+1}^{(v)}\right)_{i=1,2,3}\right]$ estimated, in turn, as hinge functions of β using one of the models (15). Tables 1 and 2 indicate the logarithmic form (single- for g_1, double- for g_2) and the coefficients of each of the parameter hinge functions $\left[q_1^{(h)}(\beta), X_{0_{1,2}}^{(h)}(\beta), \ldots\right]$. The substitution of these functions in Eqs. (13)–(14), provides the closed-form expressions of the hinge models.

Using the two-stage procedure presented above, $\hat{\overline{u_h}}(X_0, \beta)$ and $\hat{\overline{u_v}}(X_0, \beta)$ are constructed by combining two sequential hinge regressions of the LT datasets Appendix B, one performed along the spatial coordinate X_0 (Eqs. (13)–(14)) and the other along the temporal coordinate β (Eqs. (15)).

3.3. Land Subsidence due to Groundwater Abstraction

Under the assumptions of the Theis analytical solution (5), it is possible to apply the principle of linear superposition to simulate the effects of the changes in pore pressure Δp associated, for example, with multiple wells operating simultaneously and at variable pumping rates. Likewise, due to the hypothesis of linear elasticity and the boundary conditions to which the semi-infinite domain is subject, the principle of superposition can also be applied to the surface displacement fields associated with multiple overlapping Δp fields.

Considered here is the case of a generic system of n_w pumping wells operating at constant flow rates $Q_1, Q_2, \ldots, Q_{n_w}$ from the starting times $t_{s,1}, t_{s,2}, \ldots, t_{s,n_w}$, at the locations $(x_{w,1}, y_{w,1}), (x_{w,2}, y_{w,2}), \ldots, (x_{w,n_w}, y_{w,n_w})$, respectively. The surface displacement components (u_x, u_y, u_z) at the generic location (x_0, y_0) and at the time t, are given by:

$$u_x(x_0, y_0, t) = \frac{c_M \cdot (1-\nu) \cdot \rho_w \cdot g}{4 \cdot \pi^2 \cdot K} \cdot \sum_{i=1}^{n_w} Q_i \cdot \hat{\overline{u_h}}(D_{0,i}, \beta_i) \cdot \eta_{x,0,i}$$
$$u_y(x_0, y_0, t) = \frac{c_M \cdot (1-\nu) \cdot \rho_w \cdot g}{4 \cdot \pi^2 \cdot K} \cdot \sum_{i=1}^{n_w} Q_i \cdot \hat{\overline{u_h}}(D_{0,i}, \beta_i) \cdot \eta_{y,0,i} \quad (16)$$
$$u_z(x_0, y_0, t) = \frac{c_M \cdot (1-\nu) \cdot \rho_w \cdot g}{4 \cdot \pi^2 \cdot K} \cdot \sum_{i=1}^{n_w} Q_i \cdot \hat{\overline{u_v}}(D_{0,i}, \beta_i)$$

where $D_{0,i}$ and $(\eta_{x,0,i}, \eta_{y,0,i})$ represent the length and the cosine directors of the 2D vector $\left(\frac{x_0 - x_{w,i}}{c}, \frac{y_0 - y_{w,i}}{c}\right)$, respectively, and $\beta_i = \frac{S_s}{4K} \cdot \frac{c^2}{t - t_{s,i}}$ $(i = 1, 2, \ldots, n_w)$. In Eqs. (16), each of the terms in the sums need to be considered only if $t > t_{s,i}$.

The functions $\hat{\overline{u_h}}$ and $\hat{\overline{u_v}}$ are given by the LT model presented in Section 3.1 or by the hinge model presented in Section 3.2 (Eqs. (13)–(14)). Note that Eqs. (16) can also be applied to conditions where pumping rates are time-dependent. Scripts of the land subsidence simulator based on the LT model and the hinge model are available in the

Table 2
Coefficients for the logarithmic hinge functions, either $g_1(\beta)$ or $g_2(\beta)$ (Eqs. (15)), defining the dependence on β of each of the parameters in $\left[q_1^{(v)}, \left(X_{0_{i-1,i}}^{(v)}, \Delta m_{i-1,i}^{(v)}, \Delta_{i-1,i}^{(v)}\right)_{i=2,3,4}\right]$. These functions are used in Eq. (14) to construct the hinge model $\hat{u}_v(X_0, \beta)$.

Fitting parameter →	$q_1^{(v)}(\beta)$	$\Delta m_{1,2}^{(v)}(\beta)$	$\Delta m_{2,3}^{(v)}(\beta)$	$\Delta m_{3,4}^{(v)}(\beta)$	$X_{0_{1,2}}^{(v)}(\beta)$	$X_{0_{2,3}}^{(v)}(\beta)$	$X_{0_{3,4}}^{(v)}(\beta)$	$\Delta_{1,2}^{(v)}(\beta)$	$\Delta_{2,3}^{(v)}(\beta)$	$\Delta_{3,4}^{(v)}(\beta)$
Hinge model →	g_1	g_1	g_1	g_1	g_2	g_2	g_2	g_1	g_1	g_1
N	2	2	2	3	2	2	2	2	3	3
ξ_1	1.4680	−1.1470	−22.8500	1.1520	−0.5399	0.0552	0.3700	0.0725	0.4005	0.1995
η_1	−0.0703	−0.0410	0.6741	−1.6480	−0.4240	−0.5202	−0.5250	−0.2701	0.0000	0.0000
$\Delta\eta_{1,2}$	−1.6550	−1.1250	1.8730	0.2997	0.4240	0.5202	0.5250	0.2701	−0.0036	0.8089
$\Delta\eta_{2,3}$	–	–	–	5.4320	–	–	–	–	0.0036	−0.8089
$\delta_{1,2}$	3.2610	0.5345	24.2800	0.2358	2.0000	1.5010	1.4998	1.2020	0.0861	0.0411
$\delta_{2,3}$	–	–	–	0.9023	–	–	–	–	0.0861	0.0411
$\beta_{1,2}$	4.4371	0.5049	9.71×10^{-7}	0.0525	0.0581	0.9781	2.9936	0.0269	4.04×10^{-8}	1.82×10^{-3}
$\beta_{2,3}$	–	–	–	147.9108	–	–	–	–	7.55×10^{-8}	1.83×10^{-3}

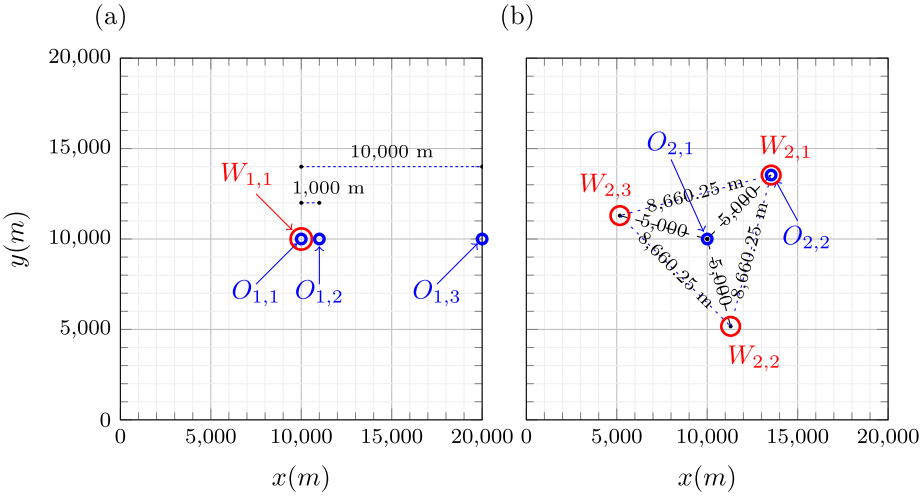

Fig. 5. Plan views of the well fields #1 (a) and #2 (b) adopted for model testing. Well field #1 includes a single well at $W_{1,1} \equiv (10,000\text{ m}, 10,000\text{ m})$. Well field #2 consists of 3 wells, $W_{2,1}$, $W_{2,2}$, and $W_{2,3}$, at the vertices of an equilateral triangle with radius 5000 m and centred at the location $W_{1,1}$. Both subpanels show the location of observation points $(O_{1,1}, O_{1,2}, ...)$ chosen to plot profiles of the displacement vs. time.

Table 3
Aquifer parameters adopted for the selected test cases. The aquifer has a transmissivity T of 400 m^2/d, and a storativity S of 3.9×10^{-2}.

c (m)	b (m)	K (m/d)	ϕ (/)	c_M (Pa^{-1})	c_w (Pa^{-1})	S_s (m^{-1})	ν (/)
200	40	10	0.25	1×10^{-7}	4.6×10^{-10}	9.8×10^{-4}	0.3

supplemental information (SI) section of this paper. The SI also includes example input files of the codes along with a detailed description of the parameters in them.

4. Model Testing

For testing purposes, a 200-m deep and 40-m thick confined aquifer is considered, with the parameters reported in Table 3. Two well field scenarios are hypothesised. Well field #1 (Fig. 5a) consists of a single large-capacity well operated continuously for 5 years at the extraction rate of 1000 m^3/d from the location $W_{1,1} \equiv$ (10,000 m, 10,000 m). Well field #2 (Fig. 5b), consists of 3 wells at the locations $W_{2,1} \equiv$ (13,535.53 m,13,535.53 m), $W_{2,2} \equiv$ (11 294.10 m, 5,170.3 m), and $W_{2,3} \equiv$ (5,170.3 m, 11 294.10 m), pumping continuously for 5 years at a flow rate of 333.33 m^3/d each. The three wells form an equilateral triangle, with a distance of 5000 m from its center, which coincides with the location $W_{1,1}$ (Fig. 5a). Note that Well field #1 and Well field #2 have the same cumulative extraction rate of 1000 m^3/d.

4.1. Single-Well Scenario

Fig. 6 shows the maps of the displacement fields u_x (subpanels a-b), and u_z (subpanels c-d) after 1825 days (5 years) of continuous operation of Well field #1 (u_y-maps are not shown as they can be inferred from a 90° rotation of the u_x maps). Subpanels 6a and b present the comparison of the u_x field obtained with the LT model and the hinge model with that determined using the FE approach as in Eq. (4). The latter is considered the most accurate approach as it relies on a high-resolution discretisation of the aquifer domain (not shown here), in which the Δp field is calculated from the Theis analytical solution (Eq. (5)) using linear superposition of effects, and the displacement components are calculated by spatial integration of the NoS Eqs. (2).

In Fig. 6a, the horizontal displacement u_x obtained with the LT model matches quite well that calculated with the FE model, particularly at "closer" distance, within about 2 km, from the pumping well, whereas some slight discrepancies are observed farther away. In Fig. 6b, the horizontal displacement u_x obtained with the hinge model still matches closely the one given by FE model, but the discrepancies become more significant, however not dramatic, away from the pumping well.

Fig. 6c and d pair the u_z fields obtained with the LT and FE model, and the hinge and FE model, respectively. In Fig. 6c, the LT model exhibits a close fidelity to the FE model in terms of u_z. Fig. 6d, shows that the hinge model is very accurate at closer distance (less than 2 km) from the pumping well, where u_z is more pronounced, but such an accuracy tends to deteriorate, although slightly, away from the well, where the displacement becomes comparatively smaller. It is interesting to observe that, when compared the FE model, both the

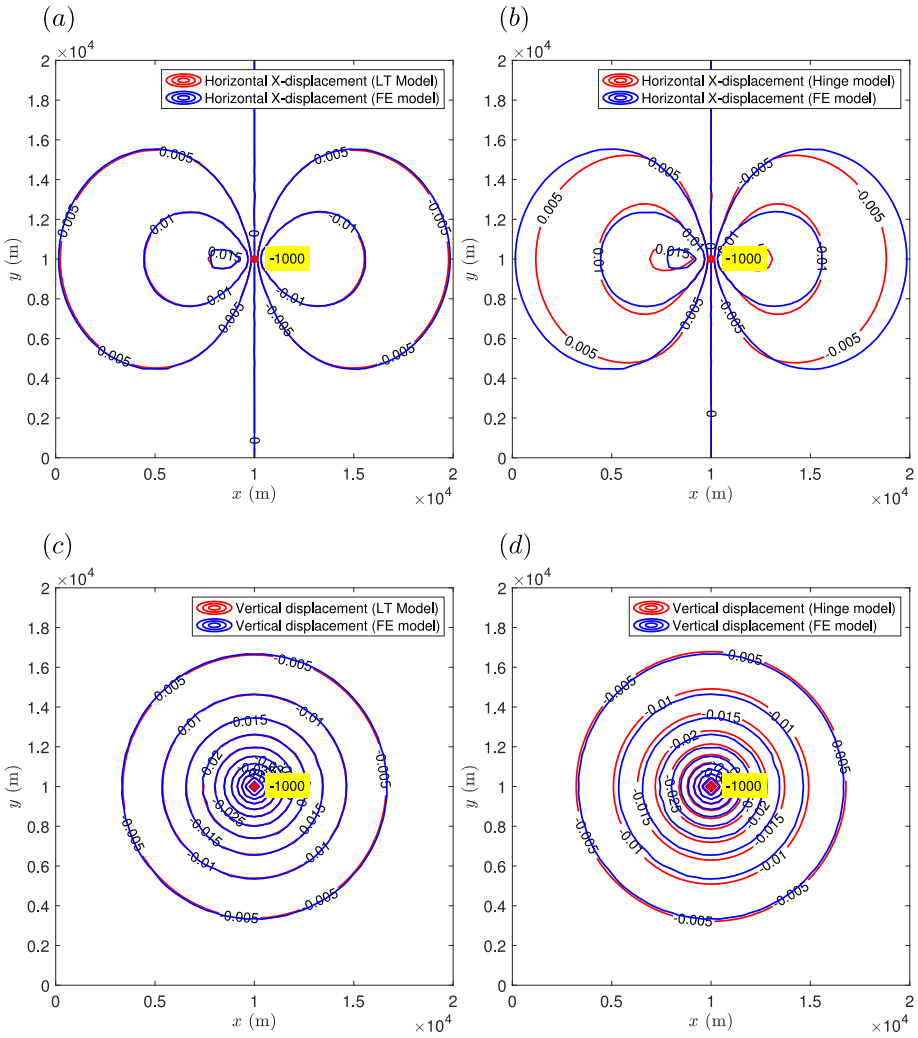

Fig. 6. Maps of the surface displacement u_x and u_z after 5 years of continuous operation of a single well extracting 1000 m^3/d. Subpanels (a) and (b) present, for purposes of comparison, the u_x fields obtained with the FE model (the same in both maps), the LT model and the hinge model, respectively. Subpanels (c) and (d) present the same comparisons for the u_z fields.

LT and the hinge models seem to mildly underestimate the horizontal displacement u_x, and mildly overestimate the vertical displacement u_z.

The results presented in Fig. 6 relate to a single value of the time-dependent variable β (5.38×10^{-4}) so that the discrepancies between the LT and hinge models and the FE model can be explained in terms of the accuracy of the two approaches with respect to the spatial variable X_0 for that β value. Overall, the LT model is generally very accurate where displacements are larger, that is, for smaller X_0, and a bit less accurate where displacements are smaller, that is, for larger X_0. This likely due to the accuracy in the numerical calculation of the integrals (9)–(10), which is apparently close to perfect for low X_0, but deteriorates — although quite slightly — for larger X_0. The hinge model is apparently less accurate than the LT model because of the propagation of errors that arise from the numerical calculation of Eqs. (9)–(10), as in the LT model, and from the hinge approximation, which is somewhat less accurate for larger X_0 values (Fig. B.12).

Fig. 7 shows the profiles of the surface displacements u_x (subpanels a-b) and u_z (subpanels c-d) vs. time over the 5 years of operation of Well field #1, at three observation points, one located at the pumping well ($O_{1,1}$ in Fig. 5a), and the other two at distance of 1 km and 10 km from the pumping well ($O_{1,2}$ and $O_{1,3}$ in Fig. 5a). Subpanels 7a and b present the comparison of the u_x profiles obtained with the LT model and the hinge model with that from the FE model. Subpanels 7c and d present a similar comparisons but for the u_z displacement component. It should be observed that these profiles refer to fixed values of the scaled distance X_0, whereas the time-dependent variable β varies between 5.38×10^{-4} and 0.2 (using the parameters in Table 3). Overall, these plots confirm that, when compared to the FE model, the LT model is slightly more accurate than the hinge model and both models tend to underestimate the horizontal displacement u_x, and overestimate the vertical displacement u_z. The absolute error between the different formulations appears to increase with time (*i.e.* as β decreases) and is more pronounced at intermediate values of the scaled distance X_0.

4.2. Three-Well Scenario

Fig. 8 presents maps of the horizontal displacement u_x (subpanels a-b), and the vertical displacement u_z (subpanels c-d) after 1825 days (5 years) of continuous operation of Well field #3 (u_y-displacement is not shown). Fig. 8a and b show that, even in the case of multiple operating wells, the LT model and the hinge model lead to u_x maps very similar to those obtained calculated with the FE model. The fidelity of the two models is particularly good at "closer" distance (~2 km or less) from the pumping wells. Discrepancies with the FE model are observed at large distance, particularly with the hinge model, which, as previously indicated, is affected by numerical integration errors (Eqs. (9)–(10)), which also affect the LT model, and approximations in the hinge regression.

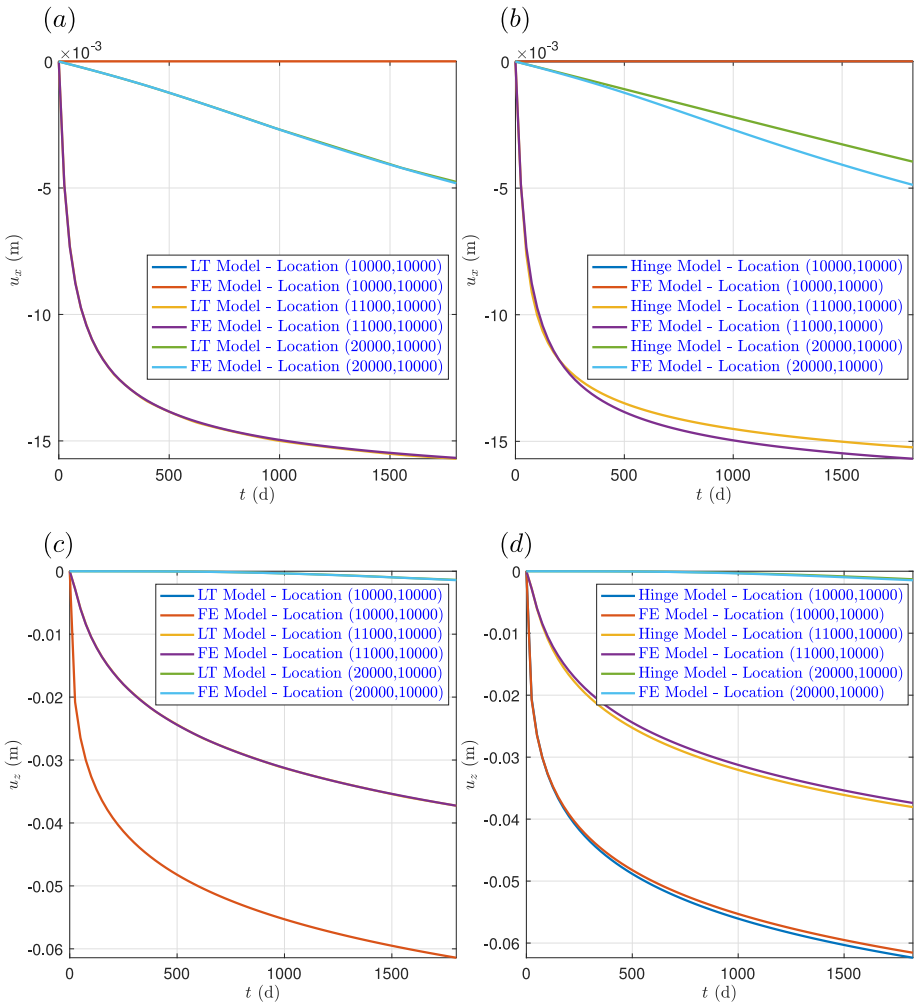

Fig. 7. Profiles of the surface displacements u_x and u_z vs. time induced by the continuous operation of a single well extracting 1000 m^3/d over 5 years. Displacements are shown at three locations, one in close proximity to the pumping well ($O_{1,1}$ in Fig. 5a), and the other two at 1 km and 10 km distance from it, respectively ($O_{1,2}$ and $O_{1,3}$ in Fig. 5a). Subpanels (a) and (b) present, for purposes of comparison, the u_x profiles obtained with the FE model (the same in both plots), the LT model and the hinge model, respectively. Subpanels (c) and (d) present the same comparisons for the u_z fields.

Subpanels 8c and d show the comparison of the u_z maps obtained with FE model with those calculated using the LT and hinge model, respectively. In Fig. 6c, the LT model matches quite well the FE model response, and appears to mildly underestimate the lateral extent of the displacement bowl. On the other hand, Fig. 6d indicates a reasonable matching between the hinge model and the FE model results, but in this case the hinge model overestimates the lateral extent of the displacement bowl, seemingly due to an overestimation of the vertical displacement introduced at larger distance (see Fig. B.12 in Appendix B.0.1).

Fig. 9 presents the evolution of the surface displacements u_x (subpanels a-b) and u_z (subpanels c-d) over the 5 years of operation of Well field #3. The displacement profiles are shown for two observation points, one located at the center ($O_{2,1}$ in Fig. 5b) of the well field, which is 5000 m away from each of the pumping wells, and another ($O_{2,2}$ in Fig. 5b) located right at pumping well on $W_{2,1}$.

Subpanels 9a and b present the comparison of the u_x profiles obtained with the LT model and the hinge model with that calculated using the FE model. It is interesting to observe that all models show $u_x = 0$ at $O_{2,1}$. This is expected, since such a point is "central" and equidistant from the three pumping wells, and thus undergoes no horizontal displacement if the latter operate at the same pumping rate. On the other hand, the u_x displacement at $O_{2,2}$ depends only on the effect of the wells at $W_{2,2}$ and $W_{2,3}$ (Fig. 5b). In Fig. 9a a reasonable match is observed between the LT model and the FE model, with the former overestimating u_x at smaller times and underestimating it at larger times. These errors, however minor, can be linked to the numerical integration of Eqs. (9)–(10). In Fig. 9b a more significant discrepancy is observed between the hinge model and the FE model, with the former generally underestimating u_x. This error is due to the combined effect of numerical errors introduced in the calculation of the integrals (9)–(10), and in the hinge regression for larger values of X_0. However, it is worth mentioning that the relevance of these errors should be considered minor as the intensity of the horizontal displacement is indeed very small due to the large distance between the two wells $W_{2,2}$ and $W_{2,3}$, and the observation point $O_{2,2}$.

Subpanels 9c and c allow for the comparison of the u_z profiles obtained with the LT model and the hinge model with those calculated using the FE model. The matching between the models is overall satisfactory, with a slightly better fidelity to the FE model of the LT model, rather than the hinge model. These discrepancies are more noticeable for observation points (*e.g.* $O_{2,1}$ in Fig. 5b) that are situated at larger distance X_0 from the pumping wells. On the other hand, when observation points (*e.g.* $O_{2,2}$ in Fig. 5b) are in close proximity to one

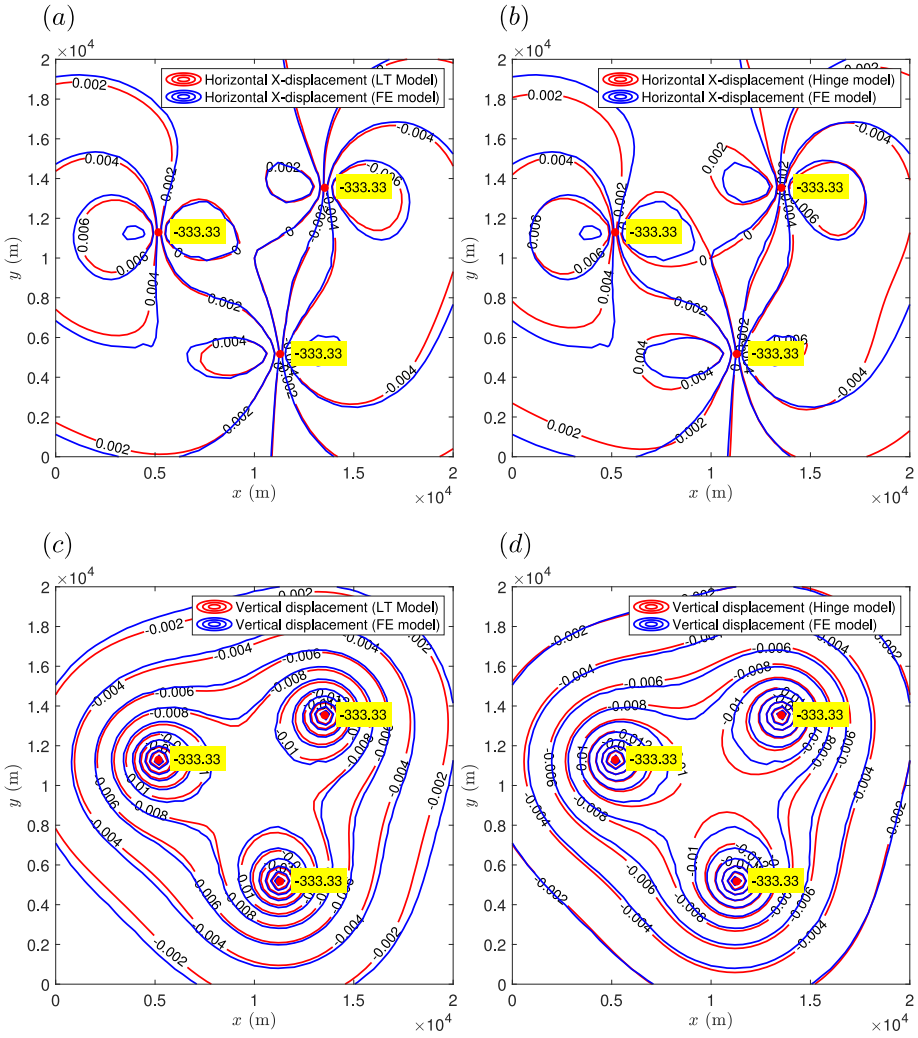

Fig. 8. Maps of the surface displacement u_x and u_z after 5 years of continuous operation of 3 wells extracting 333.33 m^3/d continuously for 5 years. The three wells are equidistant from one another (8660.25 m) and at a distance of 5000 m from the well location in Well field #1, that is, (10,000 m, 10,000 m). Subpanels (a) and (b) present, for purposes of comparison, the u_x fields obtained with the FE model, the LT model and the hinge model, respectively. Subpanels (c) and (d) present the same comparisons for the u_z fields.

of the pumping wells (*e.g.* $W_{2,1}$ in Fig. 5b) approximation errors for both LT and hinge models are smaller because u_z is due predominantly to the effect of that pumping well, and less to the contribution of the other pumping wells, which is potentially less accurate due to the large distance X_0 at which they operate from the observation point.

5. Discussion

The LT and the hinge models rely on the coupling of the classical Theis equation (5), which describes flow to a well, with the NoS equations, which quantify surface displacement caused by changes in effective stress. The assumption of linear elasticity forms the basis of the model, resulting in integral equations that can only be solved numerically, for example adopting a sufficiently resolved FE discretisation of the aquifer where pumping wells operate. However, it should be noted that FE-based methods often demand significant computational resources, and expertise to prepare model inputs and analyse results. To address these challenges, the LT and hinge model formulations proposed here aim to strike a balance between computational efficiency and accuracy and constitute approximations that can provide results comparable to the FE model.

It is important to acknowledge that these models rely on idealised representations of the subsurface system. The aquifer is assumed to be laterally unbounded, perfectly confined, horizontal, constant thickness, and homogeneous in terms of hydraulic conductivity K, vertical compressibility c_M and porosity ϕ. In addition, pumping wells are considered fully screened and point-like. While these assumptions (Theis, 1935) may not capture all the complexities of real-world aquifers, they are widely applied by practitioners for initial calculations, pumping tests, and other practical purposes for flow to pumping wells. Furthermore, the deformation of the subsurface is assumed to be caused solely by changes in effective stress, which are estimated to be equal and opposite to changes in pore pressure given by the Theis model (5). This assumption relies on Terzaghi's principle (Terzaghi and Peck, 1967) and assumes that the total stress remains constant during aquifer pumping, which is generally valid for confined aquifers. However, in the case of unconfined aquifers, the use of the Theis equation is not warranted, and the total stress does change. In these instances, it is necessary to determine how changes in effective stress can be quantified and corrected based on the changes in pore pressure, and analytical solutions distinct from Theis's equation need to be applied.

Another important matter of concern is the underlying assumption of laterally infinite aquifers. While these aquifers do not exist in reality,

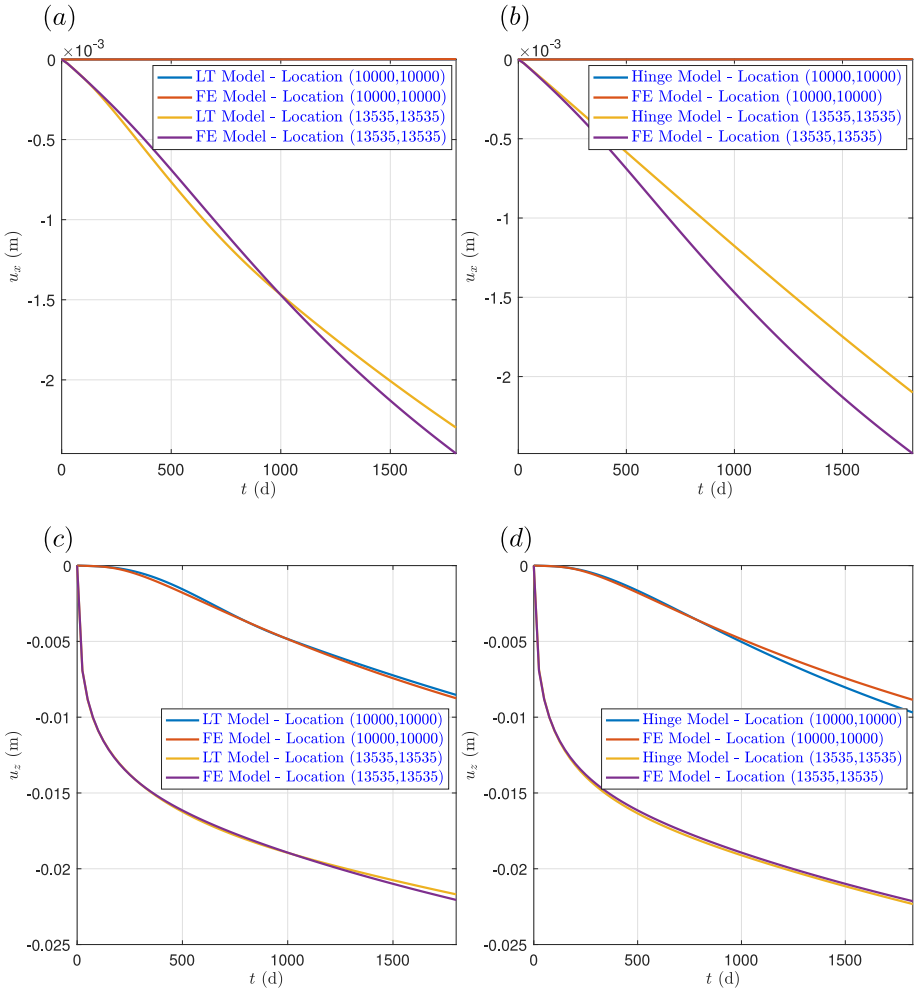

Fig. 9. Profiles of the surface displacements u_x and u_z vs. time induced by the continuous operation of 3 wells extracting 333.33 m^3/d continuously over 5 years. Displacements are reported for two observation points, one at the center of the well field ($O_{2,1}$ in Fig. 5b) and another at one of the pumping wells ($O_{2,2}$ in Fig. 5b)). Subpanels (a) and (b) present, for purposes of comparison, the u_x profiles obtained with the FE model (the same in both plots), the LT model and the hinge model, respectively. Subpanels (c) and (d) present the same comparisons for the u_z fields.

the models developed in this study should be applicable to aquifers of sufficiently "large" extent, that is, large enough that the cone of depression caused by groundwater pumping and the surface area affected by displacements remain within the physical boundaries of the system. Note that this does not depend on the boundaries alone, but also on the intensity of groundwater abstraction rates and the time horizon over which pumping occurs. Also, since the extent of the cone of depression is directly proportional to the hydraulic conductivity K of the aquifer, and inversely proportional to the specific elastic storage S_s, which depends on the vertical compressibility c_M (Eq. (6)), the boundary effects are expected to be less significant for aquifers having lower conductivity and larger storage properties, which imply smaller cones of depression and smaller surface displacement bowls.

The models developed here can be applied under the assumption the aquifer is perfectly confined, that is, bounded above and below by perfectly impervious aquicludes. As such, they do not take into account of changes in fluid pressure that may occur in confining layers, and the consequent compaction, which may result results significant under particular conditions (Ferronato et al., 2004; Zhang et al., 2020). Last but not least, while it is important to acknowledge that the models presented here have certain limitations due to the simplifying conceptualisations discussed above, their computational efficiency makes them particularly suitable for obtaining fast initial estimates related to land subsidence caused by groundwater pumping from confined aquifers, what-if analyses, assessment of groundwater pumping based on displacement observations, risk assessment, decision-making, stochastic simulations requiring repeated model runs, and simulation–optimisation based groundwater management approaches.

6. Conclusions

This paper presented innovative semi-analytical models designed for estimating land subsidence resulting from groundwater pumping in confined aquifers. Their derivation couples the NoS equations with the Theis solution, resulting in surface displacement components (horizontal and vertical) expressed as integrals that must be solved numerically, requiring significant computational effort similar to that of more advanced numerical models like FDs or FEs. The paper introduces two distinct models that aim to reduce such an effort: one utilising a lookup table (LT) containing results from numerical integration, and the other offering direct closed-form surface displacement solutions through the fitting of LT data with "hinge" models, that is, piecewise-linear functions connected by sigmoidal curves. Such solutions depend on two dimensionless spatio-temporal variables, which account for

aquifer depth and thickness, well locations, pumping schedules, and essential hydro-geomechanical properties like hydraulic conductivity, porosity, vertical compressibility of the porous skeleton, and water compressibility.

Emphasising computational efficiency and scalability through the superposition principle, these models can simulate land subsidence caused by various well pumping scenarios. To validate their accuracy, a confined aquifer with specific dimensions was considered for testing, and the model results were rigorously compared with those obtained with a finite-element-based integration of the NoS solution and Theis equation. Impressively, these models provide quite accurate predictions of land subsidence, with errors below 5% when compared to more complex models, while resulting computationally much more efficient. However, one must be aware that these models remain analytically-based and thus should be applied only within the limitations of the NoS and Theis solutions, which rely on simplified subsurface conceptualisations. As such, these models are ideally suited for swift initial assessments, what-if analyses, assisting groundwater management decisions, and stochastic simulations for risk assessment. Under these real-world settings, they offer a robust toolset for assessing and mitigating the impacts of groundwater pumping in confined aquifers, with scalability ensuring applicability across diverse hydrogeological conditions.

CRediT authorship contribution statement

Domenico Baù: Writing – review & editing, Writing – original draft, Visualization, Validation, Software, Methodology, Conceptualization.

Declaration of competing interest

The authors declare that they have no known competing financial interests or personal relationships that could have appeared to influence the work reported in this paper.

Data availability

A Supplemental Information Document in PDF format has been included.

Acknowledgements

The Authors has no financial or non-financial interests to declare that are relevant to the content of this article. This work was partially supported by the University of Sheffield and by the EPSRC grant no. EP/T018542/1. The Authors is grateful to the Journal Editors and two anonymous reviewers for their constructive comments, which helped improve the overall quality of the paper.

Appendix A. Lookup Table Data

Since the computation of the integrals (9)–(10) results computationally intensive, surrogates $\hat{\overline{u_h}}(X_0,\beta)$ and $\hat{\overline{u_v}}(X_0,\beta)$ can be constructed through a 2D interpolation of "data" compiled by numerical calculation of the integrals over the points of a regular grid in the (X_0,β) space. These data are reported in Table A.1 for $\overline{u_h}$ and in Table A.2 for $\overline{u_v}$. It is worth mentioning that the data in these tables are precisely those used to plot the profiles in Fig. 3. The data grid is based on 41 nodes along X_0 and 10 nodes along β. X_0's and β's are tabulated in the first column and in the first row, respectively, and the function values are in the table cells.

All tabulated data are log-transformed since they vary over several orders of magnitude. For any generic "input" point $[\log(X_0),\log(\beta)]$, surrogate displacement values $\left[\log\left(\hat{\overline{u_h}}\right),\log\left(\hat{\overline{u_h}}\right)\right]$ can be obtained by 2D interpolation of the $\log\overline{u_h}$ and $\log\overline{u_v}$ data at the four corner nodes of the gridblock to which the input point belongs and, if continuity in the derivatives is preferred, at the eight nodes of contiguous gridblocks.

Appendix B. Hinge Function Model

A continuous hinge function is a particular type of piecewise linear function formed by merging multiple straight lines with smoothing profiles around the intersection points (Sanchez-Ubeda and Wehenkel, 1998). A basic hinge function example is shown in Fig. B.10. Two straight lines with equations $s_1(x)=q_1+m_1\cdot x$ and $s_2(x)=q_2+m_2\cdot x$ form a piecewise-linear function, whose derivative is a step function with the discontinuity located at the intersection abscissa $x_{1,2}$. The hinge function $h(x)$ is characterised by a derivative having the "sigmoidal" form:

$$\frac{dh(x)}{dx}=m_1+\frac{m_2-m_1}{1+10^{-\frac{x-x_{1,2}}{\Delta_{1,2}}}} \tag{B.1}$$

where $\Delta_{1,2}$ is a coefficient that regulates the local curvature around $x_{1,2}$. After integrating Eq. (B.1), and imposing the "boundary" conditions $h(x)\to s_1(x)$ for $x\ll x_{1,2}$ and $h(x)\to s_2(x)$ for $x\gg x_{1,2}$ the hinge function expression results:

$$h(x)=q_1+m_1\cdot x+(m_2-m_1)\cdot\Delta_{1,2}\cdot\log(1+10^{\frac{x-x_{1,2}}{\Delta_{1,2}}}) \tag{B.2}$$

Eq. (B.2) can be extended to the case of a hinge function connecting a generic number N of segments, which gives:

$$h(x)=q_1+m_1\cdot x+\sum_{i=2}^{N}\Delta m_{i-1,i}\cdot\Delta_{i-1,i}\cdot\log(1+10^{\frac{x-x_{i-1,i}}{\Delta_{i-1,i}}}) \tag{B.3}$$

where $\Delta m_{i-1,i}=m_i-m_{i-1}$, $x_{i-1,i}$ is the abscissa of the intersection point between the straight lines "$i-1$" and "i" ($x_{i-1,i}=-\frac{q_i-q_{i-1}}{m_i-m_{i-1}}$), and $\Delta_{i-1,i}$ is the corresponding smoothness coefficient.

For piecewise log-linear functions, the hinge model (B.3) can be modified by substituting x with $\log x$, which yields:

$$h(x)=q_1+m_1\cdot\log x+\sum_{i=2}^{N}\Delta m_{i-1,i}\cdot\Delta_{i-1,i}\cdot\log\left[1+\left(\frac{x}{x_{i-1,i}}\right)^{\frac{1}{\Delta_{i-1,i}}}\right] \tag{B.4}$$

For piecewise double-log-linear functions, both x and h need to be log-transformed and, after some rearrangements, the hinge model (B.3) becomes:

$$h(x)=10^{q_1}\cdot x^{m_1}\cdot\prod_{i=2}^{N}\left[1+\left(\frac{x}{x_{i-1,i}}\right)^{\frac{1}{\Delta_{i-1,i}}}\right]^{\Delta m_{i-1,i}\cdot\Delta_{i-1,i}} \tag{B.5}$$

For any given number of segments N, the functions (B.3)–(B.5) depend each on $3\times N-1$ parameters. Since the profiles in Fig. 3 exhibit a locally linear behaviour on a double-log scale, Eq. (B.5) appears to be most appropriate to emulate, for any given value of β, the scaled displacement components $\overline{u_h}$ and $\overline{u_v}$ with respect to X_0. In particular, given the profile shapes in Fig. 3, it seems reasonable to select $N=3$ for $\overline{u_h}$ and $N=4$ for $\overline{u_v}$ (see corresponding hinge examples in Fig. 4).

In the case of $\overline{u_h}$, the profiles in Fig. 3a indicate that $m_1=1$, $m_2=0$, and $m_3=-2$ independent of β, thus $\Delta m_{1,2}=-1$ and $\Delta m_{2,3}=-2$. In this case, the hinge model (B.5) can be expressed as:

$$\hat{\overline{u_h}}(X_0,\beta)=\frac{10^{q_1^{(h)}}\cdot X_0}{\left[1+\left(\frac{X_0}{X_{0_{1,2}}^{(h)}}\right)^{\frac{1}{\Delta_{1,2}^{(h)}}}\right]^{\Delta_{1,2}^{(h)}}\cdot\left[1+\left(\frac{X_0}{X_{0_{2,3}}^{(h)}}\right)^{\frac{1}{\Delta_{2,3}^{(h)}}}\right]^{2\cdot\Delta_{2,3}^{(h)}}} \tag{B.6}$$

which depends on the five parameters $\left[q_1^{(h)},X_{0_{1,2}}^{(h)},X_{0_{2,3}}^{(h)},\Delta_{1,2}^{(h)},\Delta_{2,3}^{(h)}\right]$

In the case of $\overline{u_v}$, all the profiles in Fig. 3b are characterised by $m_1=0$ and $m_4=-3$ independent of β, and the hinge model (B.5) becomes:

$$\hat{\overline{u_v}}(X_0,\beta)=10^{q_1^{(v)}}\cdot\prod_{i=2}^{4}\left[1+\left(\frac{X_0}{X_{0_{i-1,i}}^{(v)}}\right)^{\frac{1}{\Delta_{i-1,i}^{(v)}}}\right]^{\Delta m_{i-1,i}^{(v)}\cdot\Delta_{i-1,i}^{(v)}} \tag{B.7}$$

Table A.1
Lookup table for assessing, by 2D interpolation, the value of the log-transformed displacement component $\log(\hat{\overline{u_h}})$ for any given combination (X_0, β). The tabulated data have been obtained by numerical calculation of Eqs. (9)–(10).

$\log(X_0)$	$\log(\beta)$									
	−8	−7	−6	−5	−4	−3	−2	−1	0	1
−2.0	−1.2019	−1.2021	−1.2026	−1.2043	−1.2095	−1.2260	−1.2770	−1.4277	−1.8178	−2.5593
−1.8	−1.0019	−1.0021	−1.0026	−1.0043	−1.0095	−1.0260	−1.0770	−1.2278	−1.6179	−2.3594
−1.6	−0.8020	−0.8021	−0.8027	−0.8043	−0.8096	−0.8260	−0.8771	−1.0278	−1.4180	−2.1596
−1.4	−0.6021	−0.6022	−0.6028	−0.6044	−0.6097	−0.6262	−0.6772	−0.8280	−1.2183	−1.9601
−1.2	−0.4023	−0.4025	−0.4030	−0.4047	−0.4099	−0.4264	−0.4775	−0.6284	−1.0191	−1.7614
−1.0	−0.2030	−0.2031	−0.2037	−0.2053	−0.2106	−0.2271	−0.2783	−0.4295	−0.8210	−1.5647
−0.8	−0.0046	−0.0048	−0.0053	−0.0070	−0.0122	−0.0288	−0.0802	−0.2321	−0.6259	−1.3729
−0.6	0.1914	0.1912	0.1907	0.1890	0.1837	0.1669	0.1151	−0.0387	−0.4380	−1.1930
−0.4	0.3818	0.3817	0.3811	0.3794	0.3739	0.3568	0.3037	0.1454	−0.2674	−1.0414
−0.2	0.5602	0.5600	0.5594	0.5576	0.5519	0.5338	0.4777	0.3089	−0.1358	−0.9502
0.0	0.7163	0.7161	0.7155	0.7135	0.7071	0.6871	0.6242	0.4315	−0.0829	−0.9671
0.2	0.8406	0.8404	0.8396	0.8372	0.8296	0.8056	0.7289	0.4860	−0.1607	−1.1234
0.4	0.9304	0.9301	0.9292	0.9261	0.9163	0.8848	0.7818	0.4402	−0.3952	−1.3980
0.6	0.9910	0.9906	0.9893	0.9850	0.9714	0.9270	0.7754	0.2560	−0.7359	−1.7420
0.8	1.0304	1.0298	1.0278	1.0216	1.0016	0.9349	0.6942	−0.0826	−1.1155	−2.1187
1.0	1.0554	1.0545	1.0516	1.0422	1.0117	0.9060	0.5038	−0.4923	−1.5078	−2.5092
1.2	1.0712	1.0698	1.0653	1.0509	1.0028	0.8272	0.1641	−0.8989	−1.9048	−2.9054
1.4	1.0809	1.0787	1.0718	1.0491	0.9709	0.6684	−0.2717	−1.3013	−2.3036	−3.3039
1.6	1.0867	1.0833	1.0723	1.0360	0.9050	0.3801	−0.6923	−1.7022	−2.7032	−3.7033
1.8	1.0899	1.0845	1.0670	1.0076	0.7812	−0.0453	−1.0988	−2.1026	−3.1030	−4.1030
2.0	1.0910	1.0824	1.0543	0.9551	0.5557	−0.4845	−1.5013	−2.5028	−3.5029	−4.5029
2.2	1.0903	1.0766	1.0308	0.8605	0.1832	−0.8961	−1.9022	−2.9028	−3.9029	−4.9029
2.4	1.0877	1.0657	0.9897	0.6897	−0.2694	−1.3003	−2.3026	−3.3029	−4.3029	−5.3029
2.6	1.0825	1.0468	0.9178	0.3907	−0.6918	−1.7018	−2.7028	−3.7029	−4.7029	−5.7029
2.8	1.0735	1.0148	0.7897	−0.0435	−1.0987	−2.1025	−3.1028	−4.1029	−5.1029	−6.1029
3.0	1.0585	0.9600	0.5606	−0.4844	−1.5012	−2.5027	−3.5029	−4.5029	−5.5029	−6.5029
3.2	1.0336	0.8638	0.1849	−0.8961	−1.9022	−2.9028	−3.9029	−4.9029	−5.9029	−6.9029
3.4	0.9916	0.6919	−0.2689	−1.3003	−2.3026	−3.3028	−4.3029	−5.3029	−6.3029	−7.3029
3.6	0.9190	0.3917	−0.6918	−1.7018	−2.7028	−3.7029	−4.7029	−5.7029	−6.7029	−7.7029
3.8	0.7905	−0.0433	−1.0987	−2.1025	−3.1028	−4.1029	−5.1029	−6.1029	−7.1029	−8.1029
4.0	0.5611	−0.4844	−1.5012	−2.5027	−3.5029	−4.5029	−5.5029	−6.5029	−7.5029	−8.5029
4.2	0.1851	−0.8961	−1.9022	−2.9028	−3.9029	−4.9029	−5.9029	−6.9029	−7.9029	−8.8910
4.4	−0.2688	−1.3003	−2.3026	−3.3029	−4.3029	−5.3029	−6.3029	−7.3029	−8.3029	−9.2910
4.6	−0.6919	−1.7019	−2.7028	−3.7029	−4.7029	−5.7029	−6.7029	−7.7029	−8.6914	−9.6910
4.8	−1.0987	−2.1025	−3.1028	−4.1029	−5.1029	−6.1029	−7.1029	−8.1029	−9.0914	−10.0910
5.0	−1.5012	−2.5027	−3.5029	−4.5029	−5.5029	−6.5029	−7.5029	−8.5029	−9.4914	−10.4910
5.2	−1.9022	−2.9028	−3.9029	−4.9029	−5.9029	−6.9029	−7.9029	−8.8918	−9.8914	−10.8910
5.4	−2.3026	−3.3029	−4.3029	−5.3029	−6.3029	−7.3029	−8.3029	−9.2918	−10.2914	−11.2910
5.6	−2.7028	−3.7029	−4.7029	−5.7029	−6.7029	−7.7029	−8.6920	−9.6918	−10.6914	−11.6910
5.8	−3.1029	−4.1029	−5.1029	−6.1029	−7.1029	−8.1029	−9.0920	−10.0918	−11.0914	−12.0910
6.0	−3.5029	−4.5029	−5.5029	−6.5029	−7.5029	−8.5029	−9.4920	−10.4918	−11.4914	−12.4910

Table A.2
Lookup table for assessing, by 2D interpolation, the value of the log-transformed displacement component $\log(\hat{\overline{u_v}})$ for any given combination (X_0, β). The tabulated data have been obtained from the numerical calculation of Eqs. (9)–(10).

$\log(X_0)$	$\log(\beta)$									
	−8	−7	−6	−5	−4	−3	−2	−1	0	1
−2.0	2.0145	1.9491	1.8721	1.7787	1.6604	1.5018	1.2720	0.9093	0.3179	−0.5321
−1.8	2.0145	1.9491	1.8721	1.7787	1.6604	1.5018	1.2720	0.9093	0.3179	−0.5322
−1.6	2.0145	1.9491	1.8721	1.7787	1.6604	1.5018	1.2720	0.9093	0.3177	−0.5324
−1.4	2.0145	1.9491	1.8721	1.7786	1.6604	1.5018	1.2719	0.9091	0.3174	−0.5329
−1.2	2.0145	1.9491	1.8720	1.7786	1.6603	1.5017	1.2717	0.9088	0.3166	−0.5343
−1.0	2.0144	1.9490	1.8719	1.7784	1.6601	1.5014	1.2713	0.9079	0.3146	−0.5377
−0.8	2.0142	1.9487	1.8716	1.7781	1.6597	1.5008	1.2702	0.9057	0.3095	−0.5461
−0.6	2.0137	1.9482	1.8710	1.7773	1.6586	1.4992	1.2676	0.9002	0.2969	−0.5669
−0.4	2.0126	1.9468	1.8693	1.7752	1.6559	1.4954	1.2611	0.8867	0.2662	−0.6167
−0.2	2.0099	1.9437	1.8657	1.7707	1.6499	1.4866	1.2463	0.8553	0.1940	−0.7287
0.0	2.0045	1.9374	1.8581	1.7612	1.6374	1.4683	1.2147	0.7866	0.0364	−0.9511
0.2	1.9950	1.9263	1.8447	1.7444	1.6149	1.4348	1.1548	0.6489	−0.2672	−1.3139
0.4	1.9807	1.9096	1.8244	1.7187	1.5800	1.3812	1.0528	0.3939	−0.7430	−1.7935
0.6	1.9620	1.8874	1.7974	1.6839	1.5313	1.3027	0.8887	−0.0527	−1.3145	−2.3401
0.8	1.9394	1.8605	1.7639	1.6400	1.4677	1.1923	0.6246	−0.7361	−1.9071	−2.9179
1.0	1.9134	1.8291	1.7244	1.5866	1.3863	1.0358	0.1806	−1.4519	−2.5045	−3.5089
1.2	1.8842	1.7934	1.6784	1.5222	1.2811	0.8035	−0.5828	−2.0849	−3.1035	−4.1053
1.4	1.8519	1.7532	1.6253	1.4442	1.1411	0.4320	−1.5700	−2.6960	−3.7031	−4.7038
1.6	1.8163	1.7079	1.5635	1.3477	0.9442	−0.2167	−2.2689	−3.3002	−4.3030	−5.3032
1.8	1.7769	1.6568	1.4906	1.2239	0.6452	−1.3684	−2.8903	−3.9018	−4.9029	−5.9030
2.0	1.7334	1.5984	1.4026	1.0567	0.1449	−2.4432	−3.4980	−4.5024	−5.5029	−6.5029

(*continued on next page*)

Table A.2 (*continued*).

$\log(X_0)$	$\log(\beta)$									
	−8	−7	−6	−5	−4	−3	−2	−1	0	1
2.2	1.6847	1.5306	1.2927	0.8143	−0.7805	−3.0821	−4.1009	−5.1027	−6.1029	−7.1029
2.4	1.6297	1.4502	1.1491	0.4292	−2.3847	−3.6950	−4.7021	−5.7028	−6.7029	−7.7029
2.6	1.5666	1.3520	0.9491	−0.2519	−3.2685	−4.2998	−5.3026	−6.3028	−7.3029	−8.3029
2.8	1.4928	1.2269	0.6466	−1.5822	−3.8901	−4.9016	−5.9027	−6.9029	−7.9029	−8.8910
3.0	1.4042	1.0587	0.1400	−3.4432	−4.4979	−5.5024	−6.5028	−7.5029	−8.5029	−9.4910
3.2	1.2939	0.8153	−0.8089	−4.0821	−5.1009	−6.1027	−7.1029	−8.1029	−9.0914	−10.0910
3.4	1.1499	0.4288	−2.7380	−4.6950	−5.7021	−6.7028	−7.7029	−8.6918	−9.6914	−10.6910
3.6	0.9496	−0.2557	−4.2685	−5.2998	−6.3026	−7.3028	−8.3029	−9.2918	−10.2914	−11.2910
3.8	0.6467	−1.6111	−4.8901	−5.9017	−6.9028	−7.9029	−8.8920	−9.8918	−10.8914	−11.8910
4.0	0.1394	−4.4433	−5.4979	−6.5024	−7.5028	−8.5029	−9.4920	−10.4918	−11.4914	−12.4910
4.2	−0.8118	−5.0822	−6.1009	−7.1027	−8.1029	−9.0923	−10.0920	−11.0918	−12.0914	−13.0910
4.4	−4.5102	−5.6950	−6.7021	−7.7028	−8.6924	−9.6923	−10.6920	−11.6918	−12.6914	−13.6910
4.6	−5.2685	−6.2998	−7.3026	−8.3029	−9.2925	−10.2923	−11.2920	−12.2918	−13.2914	−14.2910
4.8	−5.8901	−6.9017	−7.9028	−8.8926	−9.8925	−10.8923	−11.8920	−12.8918	−13.8914	−14.8910
5.0	−6.4979	−7.5024	−8.5028	−9.4926	−10.4925	−11.4923	−12.4920	−13.4918	−14.4914	−15.4910
5.2	−7.1009	−8.1027	−9.0928	−10.0926	−11.0925	−12.0923	−13.0920	−14.0918	−15.0914	−16.0910
5.4	−7.7021	−8.6928	−9.6928	−10.6926	−11.6925	−12.6923	−13.6920	−14.6918	−15.6914	−16.6910
5.6	−8.3026	−9.2929	−10.2928	−11.2926	−12.2925	−13.2923	−14.2920	−15.2918	−16.2914	−17.2910
5.8	−8.8929	−9.8929	−10.8928	−11.8926	−12.8925	−13.8923	−14.8920	−15.8918	−16.8914	−17.8910
6.0	−9.4930	−10.4929	−11.4928	−12.4926	−13.4925	−14.4923	−15.4920	−16.4918	−17.4914	−18.4910

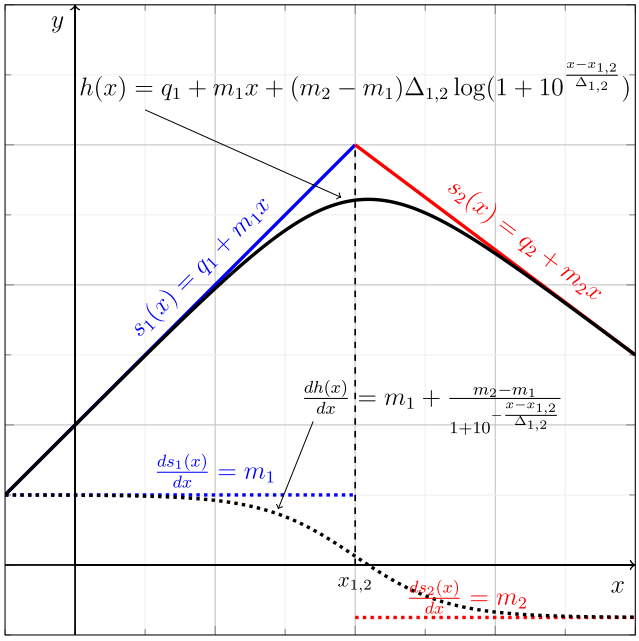

Fig. B.10. Graph of a continuous hinge function $h(x)$ (Eq. (B.3)), which smoothly connects two straight lines based on a "sigmoidal" model of the derivative $h'(x)$ (Eq. (B.1)) around the intersection point. The degree of smoothness of $h(x)$ is regulated by parameter $\Delta_{1,2}$.

which depends on the 10 parameters $\left[q_1^{(v)}, \left(X_{0_{i-1,i}}^{(v)}, \Delta m_{i-1,i}^{(v)}, \Delta_{i-1,i}^{(v)}\right)_{i=2,3,4}\right]$. Since the $\Delta m_{i-1,i}^{(v)}$ coefficients are constrained by the condition $\Delta m_{1,2}^{(v)} + \Delta m_{2,3}^{(v)} + \Delta m_{3,4}^{(v)} = -3$, the fitting parameters reduce to 9.

B.0.1. Two-Stage Fitting Analysis

Eqs. (B.6)–(B.7) explicitly show the dependency of the displacement $(\overline{u_h}, \overline{u_v})$ on the spatial variable X_0. The temporal variable β influences the hinge models through its impact on the parameter sets $\boldsymbol{\theta}_h \equiv \left[q_1^{(h)}, X_{0_{1,2}}^{(h)}, X_{0_{2,3}}^{(h)}, \Delta_{1,2}^{(h)}, \Delta_{2,3}^{(h)}\right]$ and $\boldsymbol{\theta}_v \equiv \left[q_1^{(v)}, \left(X_{0_{i,i+1}}^{(v)}, \Delta m_{i,i+1}^{(v)}, \Delta_{i,i+1}^{(v)}\right)_{i=1,2,3}\right]$. The variability of these parameters with respect to β is modelled by fitting the hinge models (B.6)–(B.7) to the profiles in Fig. 3 using a two-stage regression procedure.

In the first stage, the parameter sets $\boldsymbol{\theta}_h$ and $\boldsymbol{\theta}_h$ that guarantee the best fit of the hinge models (B.6) and (B.7) are identified for each of the β values selected in Fig. 3. For $\overline{u_h}$, the parameters in $\boldsymbol{\theta}_h$ are calculated by solving the optimisation problem:

$$\min_{\boldsymbol{\theta}_h} R_h = \sum_{i=1}^{N_s}\left\{\log\left[\frac{\hat{\overline{u_h}}(X_{0,i},\beta)}{\overline{u_h}(X_{0,i},t)}\right]\right\}^2 \tag{B.8}$$

For $\overline{u_v}$, the parameter in $\boldsymbol{\theta}_v$ are obtained by solving the optimisation problem:

$$\min_{\boldsymbol{\theta}_v} R_v = \sum_{i=1}^{N_s}\left\{\log\left[\frac{\hat{\overline{u_v}}(X_{0,i},\beta)}{\overline{u_v}(X_{0,i},t)}\right]\right\}^2 \tag{B.9}$$

The objective functions (B.8) and (B.9) quantify the square residuals between the hinge models (B.6) and (B.7), for the $N_s = 41$ scaled displacement data reported in each column of the Tables A.1 and A.2, respectively. The optimisation problems (B.8)–(B.9) are solved by means of a "trust-region-reflective" algorithm (Coleman and Li, 1996). This step is repeated for each of the β values selected in Fig. 3 and produces 10 "training" points for each fitting parameter in $\boldsymbol{\theta}_h$ and in $\boldsymbol{\theta}_v$. The resulting parameter values are plotted as "data" in Fig. B.11.

In the second stage, these training points are used to capture the relationships between the fitting parameters in $\boldsymbol{\theta}_h$ and $\boldsymbol{\theta}_v$ and the variable β. Since in Fig. B.11 the training points exhibit a fairly regular variability in relation to β, a hinge-function model such as that in Eq. (B.3) is adopted. It must be observed, however, that all profiles in Fig. B.11 use a logarithmic scale on the abscissa and, in some cases, even on the ordinate. For these reasons, the fitting models adopted in this stage must rely on either single or the double logarithmic-type hinge functions in Eqs. (B.4)–(B.5), which form the basis of the $g_1(\beta)$ and $g_2(\beta)$ models in Eqs. (15).

The regression parameters in Eqs. (15), $[\xi_1, \eta_1]$, $[\Delta\eta_{1,2}, \ldots, \Delta\eta_{N-1,N}]$, $[\delta_{1,2}, \ldots, \delta_{N-1,N}]$, and $[\beta_{1,2}, \ldots, \beta_{N-1,N}]$, are determined by applying a least-square non-linear optimisation method based on the Levenberg–Marquardt algorithm (Levenberg, 1944; Marquardt, 1963) using on the "data" in Fig. B.11. Tables 1 and 2 show the hinge model type, either $g_1(\beta)$ or $g_2(\beta)$ (Eqs. (15)), as well as the resulting number of segments N and regression parameter values.

Fig. B.12 shows a comparison between the displacement profiles $\overline{u_h}$ and $\overline{u_v}$ (Eqs. (9)) and the hinge models $\hat{\overline{u_h}}(X_0,\beta)$ and $\hat{\overline{u_v}}(X_0,\beta)$ (Eqs. (B.6)–(B.7) constructed using the two-stage regression process presented above. The fit of the hinge model to the numerical solution is generally satisfactory. Some discrepancies are typically noticeable for smaller values of β, say $\lesssim 10^{-3}$, that is, at later times, and at larger radial distance X_0.

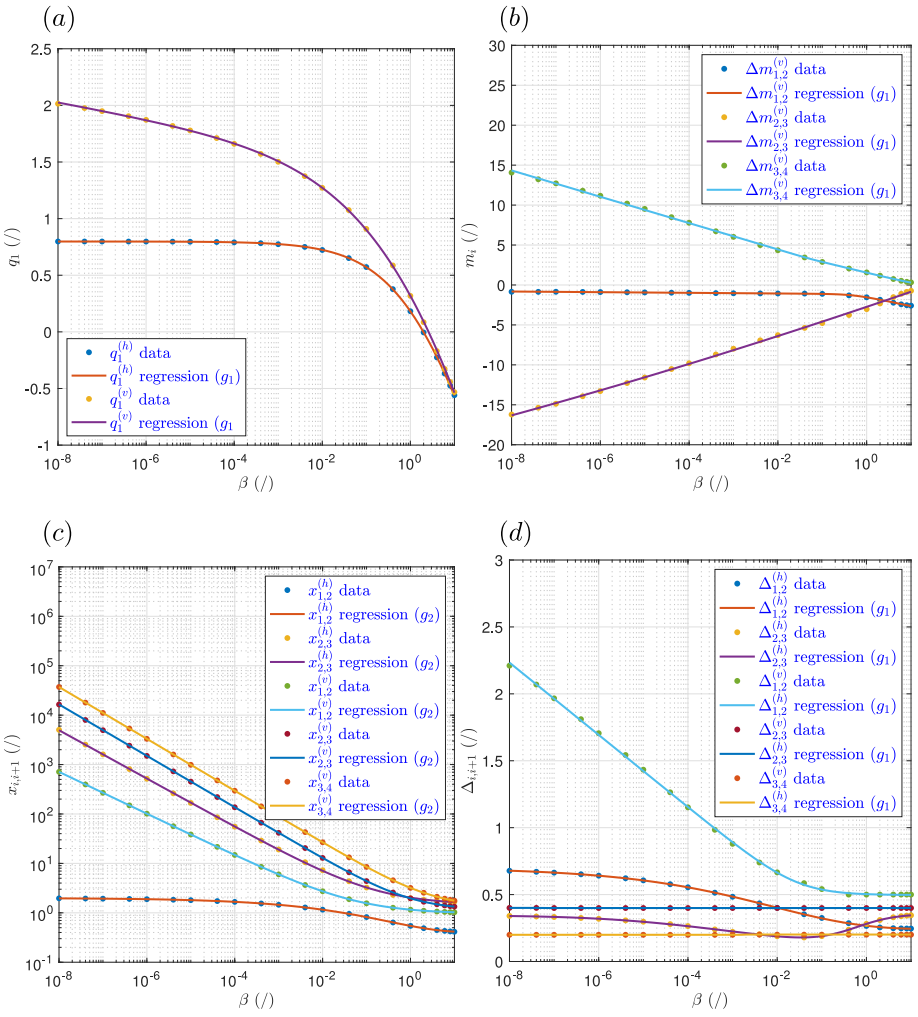

Fig. B.11. Regression parameter values ("data") for the hinge models (13) and (14) obtained for the 10 β values selected in Fig. 3. The solid lines indicate the closed-form models, either g_1 or g_2 (Eqs. (B.4)–(B.5), developed to represent the dependency of each of the regression coefficient from β.

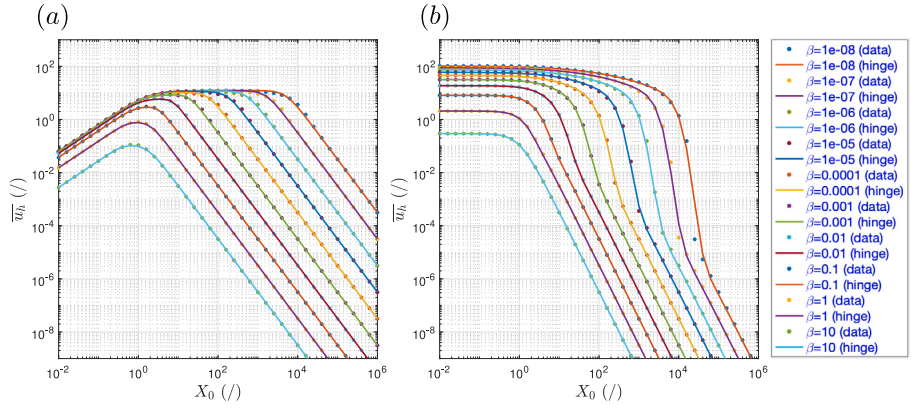

Fig. B.12. Comparison of (a) $\overline{u_h}$ against $\hat{\overline{u_h}}$, and (b) $\overline{u_v}$ against $\hat{\overline{u_v}}$ for the set of β values adopted in Fig. 3. The fit of the hinge models to the numerical solution is generally strong but some discrepancies may be observed for values of β less than 10^{-3}, and at radial distances X_0 where the displacement components start decreasing monotonically.

Appendix C. Supplementary Data

Supplementary material related to this article can be found online at https://doi.org/10.1016/j.jhydrol.2024.131813.

References

Abidin, H.Z., Andreas, H., Gumilar, I., Wibowo, I.R.R., 2015. On correlation between urban development, land subsidence and flooding phenomena in Jakarta. In: IAHS-AISH Proceedings and Reports. Copernicus GmbH, pp. 15–20.

Abramowitz, M., Stegun, I.A., 1964. Handbook of Mathematical Functions with Formulas, Graphs, and Mathematical Tables. Ninth Dover Printing, tenth gpo printing ed. Dover, New York City.

Akima, H., 1974. A method of bivariate interpolation and smooth surface fitting based on local procedures. Commun. ACM 17, 18–20.

Bear, J., Corapcioglu, M.Y., 1981a. Mathematical model for regional land subsidence due to pumping. 1. Integrated aquifer subsidence equations based on vertical

displacement only. Water Resour. Res. 17, 937–946.
Bear, J., Corapcioglu, M.Y., 1981b. Mathematical model for regional land subsidence due to pumping. 2. Integrated aquifer subsidence equations for vertical and horizontal displacement. Water Resour. Res. 17, 947–958.
Biot, M.A., 1941. General theory of three-dimensional consolidation. J. Appl. Phys. 12, 155–164.
Biot, M.A., 1955. Theory of elasticity and consolidation for a porous anisotropic solid. J. Appl. Phys. 26, 182–185.
Coleman, T., Li, Y., 1996. An interior, trust region approach for nonlinear minimization subject to bounds. SIAM J. Optim. 6, 418–445.
Corapcioglu, M.Y., Bear, J., 1983. A mathematical model for regional land subsidence due to pumping. 3. Integrated equations for a phreatic aquifer. Water Resour. Res. 19, 895–908.
de Boor, C., 1978. A Practical Guide to Splines. Springer, New York.
De Wiest, R.J.M., 1966. On the storage coefficient and the equations of groundwater flow. J. Geophys. Res. 71, 1117–1122.
Erkens, G., Bucx, T., Dam, R., de Lange, G., Lambert, J., 2015. Sinking coastal cities. Proc. Int. Assoc. Hydrol. Sci. 372, 189–198. http://dx.doi.org/10.5194/piahs-372-189-2015, URL https://piahs.copernicus.org/articles/372/189/2015/.
Ferronato, M., Gambolati, G., Teatini, P., Bau, D., 2004. Radioactive marker measurements in heterogeneous reservoirs: Numerical study. Int. J. Geomech. 4, 79–92. http://dx.doi.org/10.1061/(ASCE)1532-3641(2004)4:2(79), URL https://ascelibrary.org/doi/abs/10.1061/%28ASCE%291532-3641%282004%294%3A2%2879%29.
Galloway, D.L., Burbey, T.J., 2011. Review: Regional land subsidence accompanying groundwater extraction. Hydrogeol. J 19, 1459–1486.
Gambolati, G., Ricceri, G., Bertoni, W., Brighenti, G., Vuillermin, E., 1991. Mathematical simulation of the subsidence of Ravenna. Water Resour. Res. 27, 2899–2918.
Gambolati, G., Teatini, P., 2015. Geomechanics of subsurface water withdrawal and injection. Water Resour. Res. 51, 3922–3955. http://dx.doi.org/10.1002/2014WR016841.
Geertsma, J., 1966. Problems of rock mechanics in petroleum production engineering. In: Proceedings of 1st Cong. Int. Soc. Rock Mechan. International Society for Rock Mechanics and Rock Engineering, Lisbon, pp. 585–594.
Geertsma, J., 1973. A basic theory of subsidence due to reservoir compaction: The homogenous case. Verh. K. Ned. Geol. Mijnbouwk. Gen. 28, 43–62.
Guzy, A., Malinowska, A.A., 2020. State of the art and recent advancements in the modelling of land subsidence induced by groundwater withdrawal. Water 12, http://dx.doi.org/10.3390/w12072051, URL https://www.mdpi.com/2073-4441/12/7/2051.
Holzer, T.L., Galloway, D.L., 2005. Impacts of land subsidence caused by withdrawal of underground fluid in the United States. In: Ehlen, J., Haneberg, W.C., Larson, R.A. (Eds.), Humans As Geologic Agents. Geological Society of america, Boulder, Colorado, pp. 87–99.
Jayeoba, A., Mathias, S.A., Nielsen, S., Vilarrasa, V., Bjørnarå, T.I., 2019. Closed-form equation for subsidence due to fluid production from a cylindrical confined aquifer. J. Hydrol. 573, 964–969.
Kulp, S.A., Strauss, B.H., 2019. New elevation data triple estimates of global vulnerability to sea-level rise and coastal flooding. Nature Commun. 10, 4844. http://dx.doi.org/10.1038/s41467-019-12808-z.
Levenberg, K., 1944. A method for the solution of certain non-linear problems in least squares. Quart. Appl. Math. 2, 164–168.
Loáiciga, H.A., 2013. Consolidation settlement in aquifers caused by pumping. J. Geotech. Geoenviron. Eng. 139, 1191–1204. http://dx.doi.org/10.1061/(ASCE)GT.1943-5606.0000836, URL https://ascelibrary.org/doi/abs/10.1061/%28ASCE%29GT.1943-5606.0000836.
Marquardt, D., 1963. An algorithm for least-squares estimation of nonlinear parameters. SIAM J. Appl. Math. 11, 431–441.
Mindlin, R., 1936. Force at a point in the interior of a semi-infinite solid. Phys 7, 195–202.
Mindlin, R., Chen, D., 1950. Nuclei of strain in the semi-infinite solid. J. Appl. Phys. 21 (926), http://dx.doi.org/10.1063/1.1699785.
Pujades, E., De Simone, J., Vázquez-Suñé, E., Jurado, A., 2017. Settlements around pumping wells: Analysis of influential factors and a simple calculation procedure. J. Hydrol. 548, 225–236. http://dx.doi.org/10.1016/j.jhydrol.2017.02.040, URL https://www.sciencedirect.com/science/article/pii/S0022169417301191.
Sanchez-Ubeda, E., Wehenkel, L., 1998. The hinges model: A one-dimensional continuous piecewise polynomial model. In: Proceedings of IPMU 1998. Paris, France, pp. 878–885.
Shampine, L.F., 2008a. Matlab program for quadrature in 2d. Appl. Math. Comput. 202, 266–274.
Shampine, L.F., 2008b. Vectorized adaptive quadrature in matlab. J. Comput. Appl. Math. 211, 131–140.
Tempone, P., Fjær, E., Landrø, M., 2010. Improved solution of displacements due to a compacting reservoir over a rigid basement. Appl. Math. Model. 34, 3352–3362.
Terzaghi, K., 1923. Die Berechnung des Durchlassigkeitsziffer des Tones aus dem Verlauf der Hydrodynamischen Spannungserscheinungen. Sitzungsber. Akad. Wiss. Wien Math. Naturwiss. Kl. Abt. 2A 132, 125–138.
Terzaghi, K., Peck, R.B., 1967. Soil Mechanics in Engineering Practice, second ed. New York.
Theis, C.V., 1935. The relationship between the lowering of the piezometric surface and the rate and duration of discharge of a well using groundwater storage. Eos. Trans. AGU 16, 519–524.
Thiem, G.G., 1906. Hydrologische Methoden. J. M. Gebhardt's Verlag, URL https://cir.nii.ac.jp/crid/1130000797191951616.
van Opstal, G.H.C., 1974. The effect of base-rock rigidity on subsidence due to reservoir compation. In: IIIrd Conf. on Rock Mechanics. Denver (CO), pp. 1102–1111.
Verruijt, A., 1969. Elastic storage of aquifers. In: De Wiest, R. (Ed.), Flow Through Porous Media. Academic Press, New York, pp. 331–376.
Verrujit, A., 2015. Theory and Problems of Poroelasticity. Delft Univ. of Technology, The Netherland.
Wang, S., Zhang, Y., Liu, Z., Wen, X.h., 2022. A semianalytical formulation for estimating induced surface subsidence of a poroelastic reservoir. SPE J. 27, 3158–3177. http://dx.doi.org/10.2118/209806-PA.
Xie, K.H., Huang, D.Z., Wang, Y.L., Deng, Y.B., 2014. Axisymmetric consolidation of a poroelastic soil layer with a compressible fluid constituent due to groundwater drawdown. Comput. Geotech. 56, 11–15. http://dx.doi.org/10.1016/j.compgeo.2013.10.004, URL https://www.sciencedirect.com/science/article/pii/S0266352X13001651.
Yan, X., Yang, T., Xu, Y., Tosi, L., Stouthamer, E., Andreas, H., Minderhoud, P., Ladawadee, A., Hanssen, R., Erkens, G., Teatini, P., Lin, J., Bonì, R., Chimpalee, J., Huang, X., Lio, C.Da., Meisina, C., Zucca, F., 2020. Advances and practices on the research, prevention and control of land subsidence in coastal cities. Acta Geol. Sinica - Engl. Ed. 94, 162–175. http://dx.doi.org/10.1111/1755-6724.14403, URL https://onlinelibrary.wiley.com/doi/abs/10.1111/1755-6724.14403.
Zhang, W., Mehrabian, A., 2020. Poroelastic solution for the nonlinear injectivity of subsurface rocks with strain-induced permeability variations. Water Resour. Res. 56, e2020WR027620. http://dx.doi.org/10.1029/2020WR027620, URL https://agupubs.onlinelibrary.wiley.com/doi/abs/10.1029/2020WR027620, e2020WR027620 2020WR027620.
Zhang, Y., Yan, X., Yang, T., Wu, J., Wu, J., 2020. Three-dimensional numerical investigation of pore water pressure and deformation of pumped aquifer systems. Groundwater 58, 278–290. http://dx.doi.org/10.1111/gwat.12909, URL https://ngwa.onlinelibrary.wiley.com/doi/abs/10.1111/gwat.12909.